

The Coupled Ice Sheet–Earth System Model Bern3D v3.0

FRERK PÖPPELMEIER^{1a,b}, FORTUNAT JOOS,^{a,b} AND THOMAS F. STOCKER^{a,b}

^a *Climate and Environmental Physics, Physics Institute, University of Bern, Bern, Switzerland*

^b *Oeschger Centre for Climate Change Research, University of Bern, Bern, Switzerland*

(Manuscript received 26 February 2023, in final form 27 July 2023, accepted 30 July 2023)

ABSTRACT: Understanding climate variability from millennial to glacial–interglacial time scales remains challenging due to the complex and nonlinear feedbacks between ice, ocean, sediments, biosphere, and atmosphere. Complex climate models generally struggle to dynamically and comprehensively simulate such long time periods as a result of the large computational costs. Here, we therefore coupled a dynamical ice sheet model to the Bern3D Earth system model of intermediate complexity, which allows for simulating multiple glacial–interglacial cycles. The performance of the model is first validated against modern observations and its response to abrupt perturbations, such as atmospheric CO₂ changes and North Atlantic freshwater hosing, is investigated. To further test the fully coupled model, the climate evolution over the entire last glacial cycle is explored in a transient simulation forced by variations in the orbital configuration and greenhouse gases and aerosols. The model simulates global mean surface temperature in fair agreement with reconstructions, exhibiting a gradual cooling trend since the last interglacial that is interrupted by two more rapid cooling events during the early Marine Isotope Stage (MIS) 4 and Last Glacial Maximum (LGM). Simulated Northern Hemispheric ice sheets show pronounced variability on orbital time scales, and ice volume more than doubles from MIS3 to the LGM in good agreement with recent sea level reconstructions. At the LGM, the Atlantic overturning has a strength of about 14 Sv (1 Sv = 10⁶ m³ s^{−1}), which is a reduction by about one-quarter compared to the preindustrial. We thus demonstrate that the new coupled model is able to simulate large-scale aspects of glacial–interglacial cycles.


KEYWORDS: Ice sheets; Climate models; Model evaluation/performance


1. Introduction

Earth system models are powerful tools to investigate all aspects of climate change and have proven indispensable for the assessment of future climate scenarios (IPCC 2021). Modern fully coupled atmosphere–ocean general circulation models are approaching kilometer-scale resolution (e.g., Schär et al. 2020), but at the expense of very high computational costs. Therefore, these models are still unable to simulate slow processes in the Earth system and are limited to model integration times on the order of decades to centuries, even when employed on high-performance supercomputers. To overcome these drawbacks, reduced complexity models with substantially coarser spatial resolution have been developed [so-called Earth system models of intermediate complexity (EMICs)] that can simulate hundreds to thousands of years in a single day (Claussen et al. 2002; Stocker et al. 1992). These models usually employ simplified physics and parameterizations of the ocean and atmosphere (Edwards et al. 1998; Weaver et al. 2001) but include modules that describe slow

processes such as marine sediments and continental ice sheets (Ganopolski et al. 2010; Tschumi 2009). Their application ranges from orbital-scale paleo simulations over detailed sensitivity assessments to large ensemble simulations, and they hence fill an important gap in the hierarchy of climate models. A number of EMICs now include nearly all components of the Earth system and in particular are coupled to ice sheet models (Roche et al. 2014; Willeit et al. 2019; Ganopolski and Brovkin 2017; Fyke et al. 2011; Heinemann et al. 2014; Choudhury et al. 2020), which has opened the door for investigations of climate–ocean–ice interactions on (multiple) glacial–interglacial time scales.

Here, we describe the development of a revised version of the Bern3D EMIC. The Bern3D model is a coarse-resolution model first described by Müller et al. (2006), which is under continuous development at the University of Bern and has been extended with many additional modules and ocean tracers since its first description. Due to its low spatial resolution, the cost-efficient geostrophic–frictional balance ocean dynamics (Edwards et al. 1998), and simple energy–moisture balance atmosphere (Ritz et al. 2011a), the Bern3D model is rather fast even compared to other EMICs and capable of simulating tens of thousands of years per day. It has been used for paleoceanographic studies of the carbon cycle and its isotopes (e.g., Dincau et al. 2020; Jeltsch-Thömmes et al. 2019; Parekh et al. 2008; Menzies et al. 2012) and ocean circulation (e.g., Pöppelmeier et al. 2021c; Ritz et al. 2013, 2011a) and weathering–burial imbalances (Jeltsch-Thömmes and Joos 2023) on glacial–interglacial time scales, and extensive sensitivity tests (e.g., Pöppelmeier et al. 2021b; Rempfer et al. 2012; Ritz et al. 2011b; Pfister and Stocker 2016, 2017), but also for

 Denotes content that is immediately available upon publication as open access.

 Supplemental information related to this paper is available at the Journals Online website: <https://doi.org/10.1175/JCLI-D-23-0104.s1>.

Corresponding author: Frerk Pöppelmeier, frerk.poeppelmeier@unibe.ch

DOI: 10.1175/JCLI-D-23-0104.1

© 2023 American Meteorological Society. This published article is licensed under the terms of the default AMS reuse license. For information regarding reuse of this content and general copyright information, consult the AMS Copyright Policy (www.ametsoc.org/PUBSReuseLicenses).

Brought to you by UNIVERSITÄT BERN | Unauthenticated | Downloaded 10/02/23 11:35 AM UTC

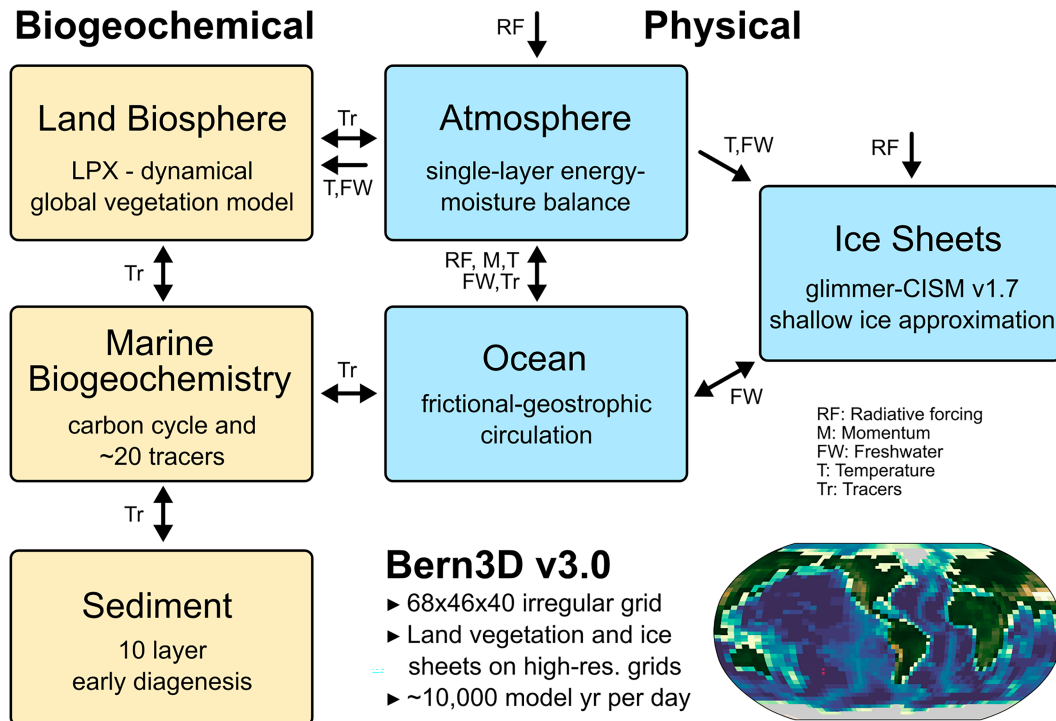


FIG. 1. Overview of model components of the Bern3D model. In the present study, only the three physical components are coupled and discussed. The model topography is shown in the lower right (see Fig. S1 for more detail).

probabilistic near-future scenario ensembles (e.g., Steinacher et al. 2013; Terhaar et al. 2022; Jeltsch-Thömmes et al. 2020), multimillennial projections (Battaglia and Joos 2018a), and data-constrained estimates of Earth system parameters (e.g., Battaglia et al. 2016; Pöppelmeier et al. 2023b).

In this study, we describe the implementation of a new, higher resolved grid and new ocean physics, and we introduce the coupling of an ice sheet model to the Bern3D model. The modern steady state of the fully coupled model is then presented in detail, and we investigate the sensitivities and feedbacks with a suite of simulations. Due to the slow processes and feedbacks, the continental ice sheets of the Northern Hemisphere never fully reached a steady-state configuration during the past 2.6 Myr. We therefore carry out a transient simulation of the entire last glacial cycle to achieve realistic ice sheet extent and volume as well as climate and ocean state of the Last Glacial Maximum (LGM), which we compare to reconstructions to assess the model's performance.

2. Model description

The Bern3D model can be divided into physical and biogeochemical components (Fig. 1). The physical modules include the ocean, atmosphere, and ice sheets, while the biogeochemistry encompasses the dynamical global vegetation model LPX (Lienert and Joos 2018) and marine biogeochemistry including a detailed implementation of the global carbon cycle (Parekh et al. 2008; Tschumi et al. 2008), as well as many additional tracers such as noble gases (Ritz et al. 2011b), CFCs

(Müller et al. 2006), N_2O (Battaglia and Joos 2018b), and geochemical tracers including their isotopes (Nd, Pa, Th, Cr, Be; Rempfer et al. 2011, 2017; Pöppelmeier et al. 2021b, 2022), and a 10-layer sediment module that couples to the biogenic particle fluxes (opal, calcite, organic) and ocean tracers (Tschumi 2009). Major updates to the biogeochemical modules of the Bern3D model will be described in a forthcoming study, while the focus of the present study is new implementations and modules of the physical components.

One of the main differences of the new version 3.0 of the Bern3D model compared to the previous version 2.0 (Roth 2013) is a new higher resolved grid. This new grid has a horizontal resolution of 68×46 cells (about $5.3^\circ \times 3.9^\circ$) compared to 41×40 of version 2.0, with an irregular spacing that allows for better resolving highly dynamic regions such as the Southern Ocean and North Atlantic that is shared between all components except for the dynamical vegetation-land biosphere and ice sheet modules, which have their own high-resolution grids. The vertical resolution of the ocean has been increased from 32 to 40 logarithmically scaled depth layers with a 31 m grid cell height at the surface increasing to 320 m at the bottom at 5000 m depth (Fig. S1 in the online supplemental material). The Bering Strait is open and only one grid cell deep and wide and thus only allows for barotropic transport. As in previous versions of the Bern3D model, the Drake Passage has been widened, and the sill depth between Greenland and Scandinavia has been increased in order to enhance the Antarctic Circumpolar Current and North Atlantic Deep Water (NADW) formation, respectively. Due to the

reduced complexity of the model the time step of the model is rather long with ~ 3 days (120 steps per year), which is also the coupling frequency between the individual physical modules except for the ice sheet, which is coupled once a year.

The ocean module forms the core of the Bern3D model and consists of a rigid-lid geostrophic–frictional balance model [see Edwards et al. (1998) and Müller et al. (2006) for details] with an isopycnal-diffusion scheme and Gent-McWilliams parameterization of eddy-induced transport (Griffies 1998) that is also employed in other models of similar complexity [e.g., GENIE (Holden et al. 2016) and CLIMBER-X (Willeit et al. 2022)]. Since the rigid-lid parameterization does not allow for dynamically changing the sea level, freshwater fluxes are implemented as virtual salinity fluxes. For diagnostic purposes we employ ideal age and artificial dye tracers as described in Pöppelmeier et al. (2021c). The ocean is coupled to a thermodynamic sea ice component and a single-layer, two-dimensional energy moisture balance atmosphere (Ritz et al. 2011a). Because of the reduced complexity atmosphere, wind fields are not dynamically calculated and instead wind stress and cloud cover are prescribed from present-day monthly climatologies (Kalnay et al. 1996). Here, we further introduce a continental ice sheet model that is coupled to the atmosphere and ocean as described in detail in section 2b.

On the technical side, we added a number of code optimizations, such as replacing matrix solvers with specialized routines, and added support for shared memory parallelization via the OpenMP standard. We were thus able to compensate for the increased runtime due to the higher resolved grid and increased complexity of the physics, and the model now integrates about 10 kyr in 1 day when all components are coupled (including biogeochemistry, sediments, and LPX-land biosphere) on eight CPUs of a high-performance computer. Without the biogeochemistry modules the runtime efficiency is increased by a factor of about 6.

a. Update of ocean physics

Two important aspects of ocean physics have been revised for the new version of the Bern3D model, namely diapycnal diffusion and brine rejection during sea ice formation. Previously, diapycnal diffusivity was prescribed in the Bern3D model with a uniform value (default: $K_d = 2 \times 10^{-5} \text{ m}^2 \text{ s}^{-1}$) that was spatially and temporally constant (Roth 2013). This, however, is a major simplification especially for paleo-simulations on glacial–interglacial time scales when sea level changed substantially. This critically impacts the spatial distribution of tidal energy dissipation and thus diapycnal diffusivity (e.g., Wilmes et al. 2019).

To improve the parameterization in the Bern3D model, we adopted the implementation by St. Laurent et al. (2002) that describes the spatially varying diapycnal diffusion according to

$$K_d = K_{bg} + \frac{\Gamma \varepsilon}{N^2}, \quad (1)$$

with the globally constant background diffusivity $K_{bg} = 2 \times 10^{-5} \text{ m}^2 \text{ s}^{-1}$, the buoyancy frequency $N^2 = g/\rho \times d\rho/dz$, the

mixing efficiency $\Gamma = 0.2$, and the turbulent energy dissipation rate ε . Equation (1) only explicitly considers tidally driven mixing and all other sources of mixing are thus included in the background diffusivity. We specifically account for the diurnal and semidiurnal tidal constituents (TC) of the energy dissipation rate as described by Schmittner and Egbert (2014) and their subgrid-scale bathymetry scheme

$$\varepsilon = \frac{1}{\rho} \sum_{z' > z}^H \sum_{\text{TC}} q_{\text{TC}} E_{\text{TC}}(x, y, z') F(z, z'), \quad (2)$$

where ρ is density, q_{TC} is local tidal dissipation efficiency, $E_{\text{TC}}(x, y, z')$ is the energy flux of the TC at longitude x , latitude y , and at all depths z' below z and above the seafloor, and $F(z, z')$ is a shape function describing the vertical decay of turbulence from the seafloor

$$F(z, z') = \frac{e^{(-z'-z)/\zeta}}{\zeta(1 - e^{-z'/\zeta})} \quad (3)$$

with $\zeta = 500 \text{ m}$. The energy dissipation rates of the four major tidal constituents (diurnal: K1 and O1, and semidiurnal: M2 and S2) are taken from the OTIS tide model using the solution of Wilmes et al. (2019) for the present day and the LGM and scaled between these fields [see section 2c(2)].

Second, we added a simple parameterization of brine rejection during sea ice formation to improve the sea surface salinity of polar regions compared to observations and stimulate more realistic deep water formation particularly around Antarctica. For this a fraction of the salt rejected during sea ice formation (here $f = 0.8$) is directly injected into the subsurface two grid cells below the surface box corresponding to a depth of about 80 m instead to the surface layer as in the previous model version. This depth roughly coincides with the upper boundary of the halocline in the Arctic (Rudels et al. 2004), which has been shown to be the depth to which brines are able to penetrate (Nguyen et al. 2009). Here we assume similar conditions for the Antarctic. If the brine injection leads to an unstable water column, the convection scheme as described by Müller et al. (2006) removes any instabilities. Brine rejection is not allowed to take place in the Hudson Bay as its very shallow depth and restricted water mass exchange with the Labrador Sea would lead to unrealistic vertical salinity gradients.

With these updates of the ocean physics, we simulate realistic deep water formation and meridional overturning such that no freshwater correction fluxes are required anymore for this revised version 3.0 of the Bern3D model. Updated ocean parameters are listed in Table S1.

b. Ice sheet coupling

We coupled the ice sheet model glimmer-CISM v.1.7 (Rutt et al. 2009) to the Bern3D model. Since our goal for the coupled model is the ability to simulate multiple glacial–interglacial cycles fully transiently with synchronous coupling, we had to achieve maximum computational efficiency of the ice sheet model and employ well-established approximations for the ice evolution and surface mass balance. Glimmer-CISM

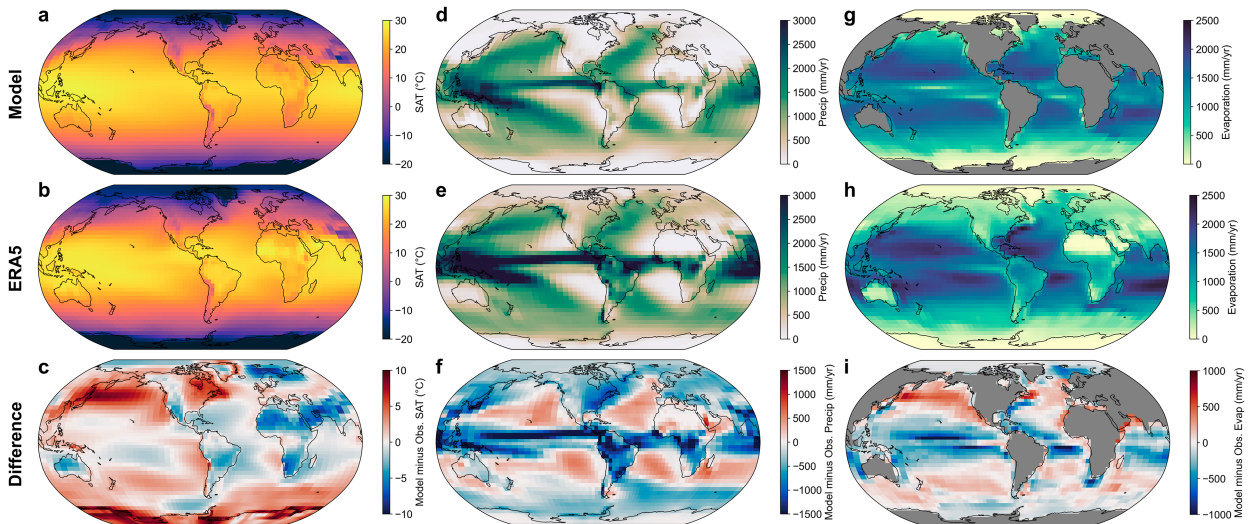


FIG. 2. Modern (a)–(c) surface atmospheric temperatures, (d)–(f) precipitation, and (g)–(i) evaporation. (top) Bern3D results for the pre-industrial, (middle) ERA5 data, and (bottom) the difference between Bern3D and ERA5.

is a 3D thermomechanic ice sheet model currently developed as part of the Community Earth System Model–CESM (Lipscomb et al. 2019). While from v.2.0 onward glimmer-CISM includes higher-order dynamical cores (Lipscomb et al. 2019), we here use the original shallow ice approximation of v.1.7 that is also employed for coupling with other reduced complexity Earth system models (e.g., FAMOUS; Gregory et al. 2012) to increase computational efficiency. However, we note that coupling with v2.1 of glimmer-CISM with the depth-integrated viscosity solver has also been successfully tested, and switching between both ice sheet model versions is fully supported as both ice sheet model versions support the same coupling interface. This facilitates future investigations that require higher order ice physics (computational costs increase by a factor of >20 for the ice sheet model v2.1 alone).

Even though ice shelves are not explicitly simulated here, the model allows for the ice sheet to advance into shallow waters. This advance is determined by a threshold water depth or flotation criterion setting the limit of grounded ice. All ice that exceeds this threshold is calved. For all simulations we here use the threshold water depth option that is further modulated by changes in sea level allowing for the ice sheets to advance beyond the present-day coastline. Since the Bern3D model has a rigid-lid ocean, we use global mean sea level reconstructions to determine water depths for the ice sheet model during transient simulations. The discrepancies in coastline caused by the different sea level stands of both model components are not resolved on the ocean grid of Bern3D due to its coarse resolution.

To test the ice sheet model under present-day boundary conditions, we set up a single grid domain only encompassing Greenland. The grid has a resolution of $20 \times 20 \text{ km}^2$ on a stereographic projection with 76×141 grid cells. For simulations of the entire last glacial cycle we run the ice sheet model on two discontinuous domains that can in principle be forced with two different parameter sets; we applied here virtually

identical sets in both domains (Table S2). The first makes up North America, Greenland, and Iceland, which we refer to as the North American ice sheet. The second is centered around Eurasia, and thus includes the Fennoscandian and British ice sheets, which we call the Eurasian ice sheet. Both ice sheet instances have a $30 \times 30 \text{ km}^2$ grid resolution on a Lambert azimuthal equal-area projection with 190×180 and 100×140 grid cells, respectively. The ice sheet model is run with a 0.5-yr time step and with 11 σ levels. Isostatic adjustment is considered assuming an elastic lithosphere and a relaxing mantle with a characteristic relaxation time constant of 2000 years. Both ice sheets are initialized with present-day bedrock topography that is derived from the ETOPO1 dataset (NOAA 2009) and bilinearly regridded to the ice sheet grids. While the Eurasian ice sheet is initialized with ice-free conditions, the North American ice sheet is initialized with Greenland's modern ice thickness (Morlighem et al. 2014).

Basal sliding is spatially variable and depends on the subglacial sediment thickness following the approach by Gregoire et al. (2012). For this we regridded the sediment thickness map by Laske and Masters (1997) on the North American and Eurasian ice sheet grids and set the basal sliding coefficient to $1.0 \text{ mm yr}^{-1} \text{ Pa}^{-1}$ where the sediment thickness is less than 20 m representing bedrock conditions, and to $7.5 \text{ mm yr}^{-1} \text{ Pa}^{-1}$ elsewhere in North America and $10 \text{ mm yr}^{-1} \text{ Pa}^{-1}$ in Eurasia (Fig. S2). Due to the highly uncertain observations of the geothermal heat flux and to keep the simulation setup relatively simple we here chose a spatiotemporally uniform value of 0.05 W m^{-2} (Sclater et al. 1980).

The large differences in spatial resolution between the ice sheet model and Bern3D constitute a major conceptual challenge for the coupling between both models. Moreover, the simplified atmosphere of the Bern3D model is unable to fully capture surface atmospheric temperature (SAT) and precipitation distributions in good agreement with modern observations (Fig. 2). To reduce these biases, we therefore force the ice sheet model with monthly mean ERA5 SAT and

precipitation fields. For simulations with climates different to modern, we then add the Bern3D SAT and precipitation anomaly fields relative to the preindustrial to the ERA5 fields. Precipitation is assumed to always fall as snow. The up- and downscaling procedures between both grid resolutions are described by [Rutt et al. \(2009\)](#) and take into account the high-resolution topography of the ice sheet model by adjusting the temperature using a prescribed lapse rate, while not adjusting precipitation. We here assume this lapse rate is spatially uniform, but temporally variable on orbital time scale. Because of the large shifts in climate and hence relative humidity over the ice sheets on these time scales, the lapse rate varies with ice sheet volume assuming a value of 5.5 K km^{-1} during full interglacials (i.e., close to the wet lapse rate) and 7.0 K km^{-1} during glacial maxima, thus taking into account the generally drier conditions ([Bartlein et al. 2011](#)).

The surface mass balance is calculated with an annual positive-degree-day (PDD; [Reeh 1991](#)) scheme from the downscaled SAT and precipitation fields. The PDD scheme assumes that the daily air temperature variation is sinusoidal with additional random interdaily fluctuations, which are normally distributed with standard deviation σ_{dd} . The sum of positive degree-days is then given by

$$\text{PDD} = \frac{1}{\sigma_{\text{dd}} \sqrt{2\pi}} \int_{\text{yr}} \int_0^{\infty} T \exp \left[\frac{-(T - T_m)^2}{2\sigma_{\text{dd}}^2} \right] dT dt, \quad (4)$$

where T_m is the monthly mean temperature. Since the scheme allows for different snow and ice melt rates, refreezing of meltwater in the firn is additionally parameterized. Up to 60% of meltwater is allowed to refreeze in the firn column if the snow layer is able to absorb it. The net surface mass balance is thus the difference between annual precipitation and the sum of snow and ice melt. All ice sheet and PDD parameters are listed in Table S2.

Since we force the ice sheet model with ERA5 plus Bern3D anomaly fields, freshwater fluxes (precipitation and runoff) are not conserved between both model components. To still account for the freshwater relocation to the continental ice sheets, we uniformly remove the freshwater from the global surface ocean that is required for the buildup of the ice sheets. Meltwater runoff, on the other hand, is routed either into the Gulf of Mexico when the North American ice sheet extends south of 50°N or to the North Atlantic (with a small fraction ($\sim 17\%$) routed to the North Pacific; Fig. S3).

After every coupling time step of 1 year the orography and albedo of the Bern3D model are updated based on the ice sheet evolution. For this, the ice sheet model calculates the fractional ice coverage of the Bern3D grid cells, which is then multiplied with a fixed value for the ice albedo of 0.6 to derive the ice sheet albedo. A value of 0.25 is assigned to snow- and ice-free ground, representative of the average mid- to high-latitude albedo. The Bern3D model further calculates snow albedo changes (see Text S1 in the online supplemental material), here for the ice-free fraction. These contributions are added up to determine the total surface land albedo, which is limited to values ≤ 0.77 . For the hypothetical case

where no ice sheet instance covers Greenland, it is assigned the present-day albedo as derived from satellite data of MODIS.

c. Model experiments

We here performed a number of simulations to characterize the behavior of the coupled model under various boundary conditions. These include steady-state as well as transient simulations that aim at demonstrating the possible applications of the coupled Bern3D model and also highlight the climate–ocean–ice interactions on glacial–interglacial time scales.

1) PREINDUSTRIAL BOUNDARY CONDITIONS AND SENSITIVITY TESTS

First, the model was spun up without interactive ice sheets under preindustrial (1765 CE) boundary conditions over 35 kyr until an equilibrium state was reached. For this, greenhouse gas concentrations were set to $\text{CO}_2 = 278 \text{ ppm}$, $\text{CH}_4 = 722 \text{ ppb}$, and $\text{N}_2\text{O} = 273 \text{ ppb}$. The Greenland ice sheet was then initialized with present-day ice thickness and the coupled model was run for another 1 kyr, but with asynchronous coupling that accelerates the ice sheet evolution by a factor of 50 (i.e., 50 000 ice sheet model years). This was deemed feasible because the Greenland ice sheet volume and extent changes only marginally, and thus the climate state does virtually not change due to climate–ocean–ice feedbacks.

Further, we performed three sensitivity tests under preindustrial boundary conditions, but with atmospheric CO_2 concentrations abruptly halved, doubled, or quadrupled at the beginning of the experiments. These simulations were run for 50 kyr with synchronous coupling to the Greenland ice sheet. This was enough to reach equilibrium states of the ocean–climate system as well as the Greenland ice sheet.

To assess the transient responses to gradual CO_2 increases, we perform six experiments for which we increase the atmospheric CO_2 concentrations by 0.5%, 1%, and 2% yr^{-1} starting from the preindustrial control. The CO_2 concentrations increase until they are either doubled or quadrupled, with constant concentrations afterward. The simulations are run for 2500 years with a synchronous coupling to the ice sheet.

Finally, we investigate the potential hysteresis behavior of the Atlantic meridional overturning circulation (AMOC) by slowly increasing freshwater hosing fluxes added to the North Atlantic (Fig. S3) in two experiments with rates of 0.02 and 0.04 Sv kyr^{-1} ($1 \text{ Sv} \equiv 10^6 \text{ m}^3 \text{ s}^{-1}$) up to a maximum hosing flux of 0.4 Sv, which was then reduced at the same rates. Further, transient step-like hosing experiments were performed. Starting from the preindustrial control, freshwater hosing fluxes between 0.1 and 0.4 Sv were applied to the North Atlantic (Fig. S3) for 500 years. These hosing fluxes were not compensated for elsewhere.

2) SIMULATING THE LAST GLACIAL CYCLE

Ice sheets respond to climate forcing on multimillennial time scales, and the Northern Hemispheric ice sheets were hence never in a fully equilibrated state during past glacial–interglacial cycles. A fair comparison between modeled and reconstructed ice sheets, for instance at the LGM, therefore

requires transiently and interactively simulating an entire glacial–interglacial cycle. We therefore simulated the last 130 kyr starting from the last interglacial. The simulation was continued from the preindustrial, which encompasses slightly different boundary conditions than the last interglacial, and we hence only evaluate the last 120 kyr of the model run. The model was forced with orbital variations (Berger 1978) and reconstructed greenhouse gas concentrations (Köhler et al. 2017). Changes in radiative forcing due to variable atmospheric dust loading were prescribed by converting the Antarctic dust record from Dome C (Lambert et al. 2012) to top-of-the-atmosphere radiative forcing. For this, the dust record was normalized to values between 0 and -2 W m^{-2} , which corresponds to an average radiative forcing of about -1 W m^{-2} at the LGM and virtually none during the Holocene.

For transient changes in wind stress, we follow the approach of Pöppelmeier et al. (2021c, 2023b). In brief, LGM wind stress anomalies from PMIP3 (Muglia and Schmittner 2015) are added to the present-day climatology and are scaled based on the benthic $\delta^{18}\text{O}$ record by Lisiecki and Stern (2016) or simulated ice volume, such that the total anomalies are added during the LGM and fractions thereof are added during intermediate climate states. We note that this is a simplification as it does not directly take into account the shape of the ice sheet, which is important for both the direction and strength of the wind stress. Similarly, the global fields of energy dissipation rates of the four tidal constituents, used to calculate diapycnal diffusivity, are scaled between their present day and LGM fields either based on the benthic $\delta^{18}\text{O}$ record or simulated ice sheet volume. There is virtually no effect of switching between both options as benthic $\delta^{18}\text{O}$ and simulated ice volume evolve closely over glacial cycles. The general impacts of these parameterizations on the global climate and ocean circulation are documented in detail in Pöppelmeier et al. (2021c). Moreover, the lapse rate is scaled between the LGM and interglacial values (see section 2b) based on the simulated ice sheet volume. Sea level as seen by the ice sheet model is prescribed after Lambeck and Chappell (2001). Since changes in insolation are not taken into account in the PDD scheme for calculating the surface mass balance (Bauer and Ganopolski 2017), we further modify the summer temperature seen by the ice sheet model. For this, we normalized the summer insolation at 65°N (Berger and Loutre 1991) (note that this is different from the orbital forcing to the atmosphere) to values between -3.6° and 2.4°C over the last glacial cycle and added these temporally evolving anomalies following the insolation to the summer temperatures applied to the ice sheet model.

3. Preindustrial climate state

a. General climate state, including the ice sheet

Under preindustrial boundary conditions the model simulates a global mean surface temperature (GMST) of 14.8°C . Regional biases in surface atmospheric temperatures are largest at high latitudes; in particular, simulated temperatures over Antarctica and the North Pacific are too warm by up to

10°C , while the Nordic seas are too cold by about 5°C (Fig. 2c). The latter can be explained by North Atlantic Deep Water formation taking place too far south in the model compared to observations. Hence, the meridional heat transport to the Nordic seas is too small in the model. Further, temperatures over large deserts, such as the Sahara, Namib, or Australian deserts, are too low. In contrast, the bias in precipitation is concentrated in the tropics, where precipitation is underestimated. Elsewhere, precipitation is generally overestimated over the ocean (except for the Southern Ocean) and underestimated over land. These biases are similar to the ones in the previous model version (Ritz et al. 2011a) and are related to the simplified parameterization of zonal and meridional moisture diffusion in the atmosphere that remained unchanged between the model versions.

Because we drive the ice sheet model with ERA5 climatologies plus Bern3D anomalies, the biases in atmospheric temperature and precipitation are not transferred to the ice sheet model. With these ERA5 climatologies the Greenland ice sheet is hence simulated reasonably well (Fig. 3), despite the simplified ice physics, basal sliding, and geothermal heat parameterizations. In general, the ice sheet extends too far to the coast, in particular in the southwestern and eastern part, most likely because fjords are not resolved at this relatively coarse resolution and fast ice streams are not parameterized, limiting the calving flux. At the center of the ice sheet the simulated ice thickness bias is less than 250 m, and both ice extent and volume of the model ($1.8 \times 10^6 \text{ km}^2$ and $3.4 \times 10^6 \text{ km}^3$, respectively) are only about 13% larger than the observational data indicate ($1.6 \times 10^6 \text{ km}^2$ and $3.0 \times 10^6 \text{ km}^3$, respectively; Morlighem et al. 2014). Surface ice speeds (Fig. 3c) are also simulated reasonably well with the characteristic slow-flowing ice in the interior of the ice sheet and fast-flowing glacier outlets along the margins represented fairly accurately (see Joughin et al. 2010). Yet, very fast flowing ice, as for instance the Northeast Greenland Ice Stream, is only poorly simulated, a model deficit that is also found in more complex ice sheet models (e.g., Lipscomb et al. 2019).

b. Ocean state

As expected, sea surface temperature (SST) anomalies mirror the ones of SAT, while simulated sea surface salinity (SSS) is generally too fresh compared to observations (Fig. S4). In the Arctic Ocean SSS anomalies form a dipole pattern with too high values in the western part and too low values in the Nordic seas, which again is related to deep water formation taking place too far south. Saline and warm Atlantic water is unable to penetrate deep into the Nordic seas and is already convected mainly south of Iceland. This structural bias of the model physics is further responsible for the too-warm global deep ocean (Fig. 4b), which yields a global mean ocean temperature (MOT) of 4.7°C . The largest subsurface warm bias is found in the South Atlantic at around 1 km water depth and is caused by Antarctic Intermediate Water (AAIW) penetration being too weak with the AAIW extent being too shallow and not reaching across the equator. This causes an even more pronounced bias in salinity in the same region (Fig. 4d) as

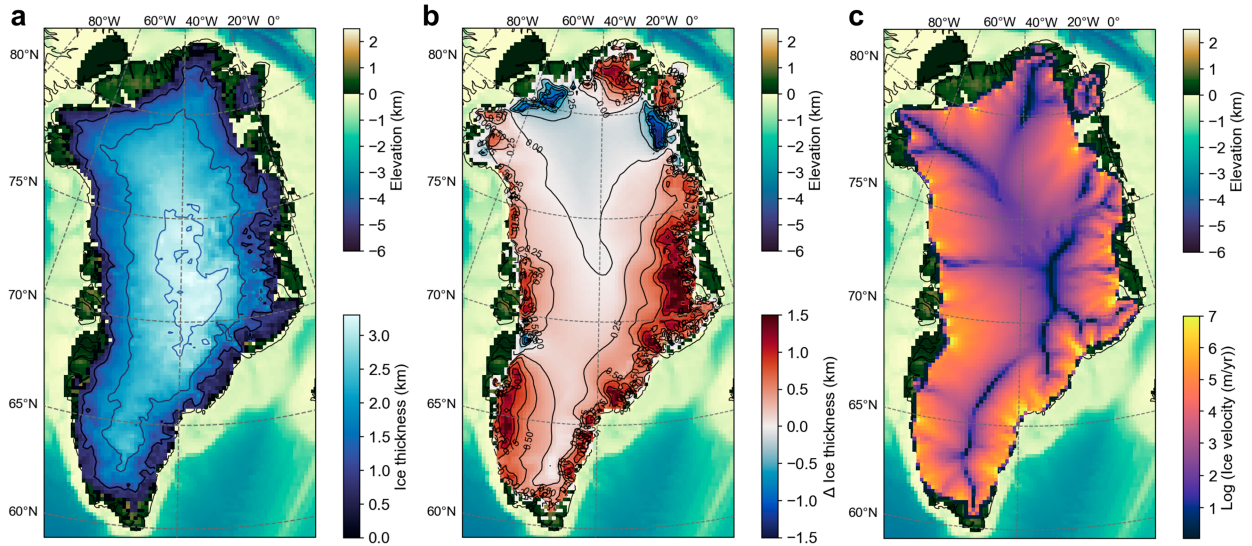


FIG. 3. Greenland ice sheet results from a simulation with a $20 \times 20 \text{ km}^2$ grid resolution integrated over 50 kyr with constant PI boundary conditions. (a) Ice thickness with contour lines every 1 km. (b) Difference of simulated ice thickness compared to present day (Morlighem et al. 2014). (c) Log_{10} of ice velocity magnitude.

the difference between AAIW and NADW salinities is markedly stronger than in temperature. Elsewhere, deep ocean salinity is simulated within <0.1 PSU compared to observations and hence in good agreement.

Deep ocean ventilation ages (as inferred from the ideal age tracer) strongly increase from the Southern Ocean toward the North Pacific where ventilation ages of more than 1000 years are reached. The vertical age distribution of the modern

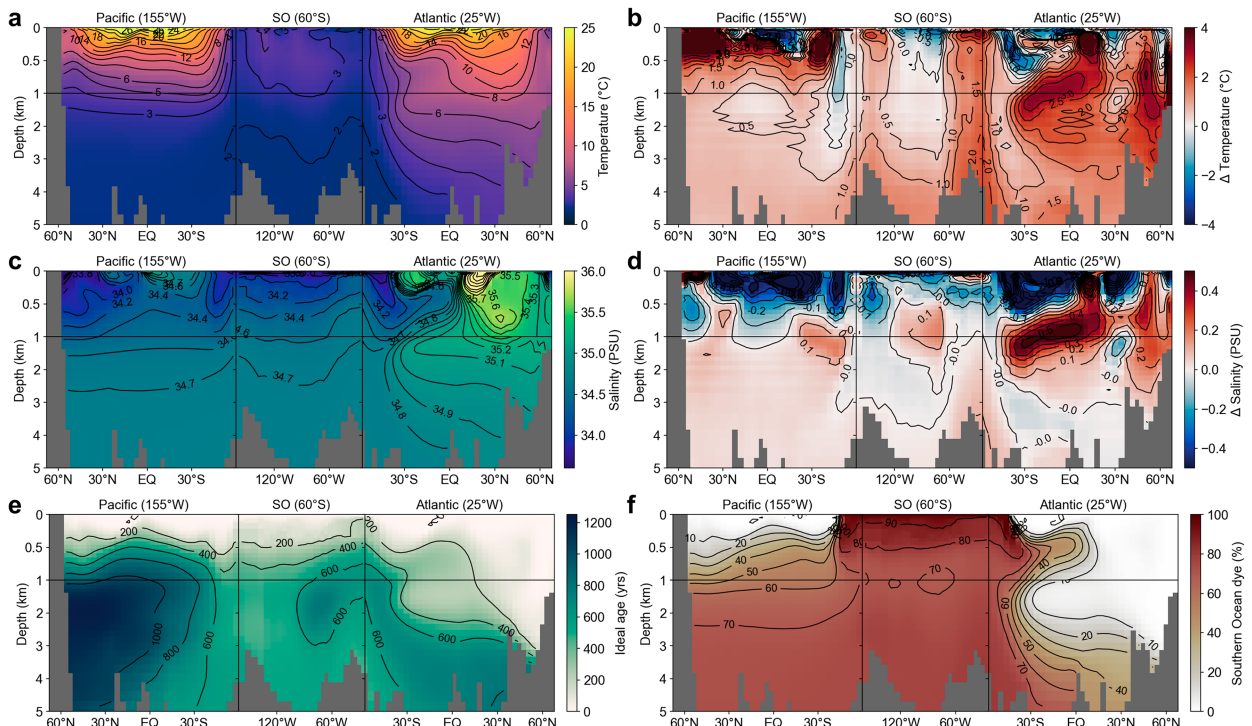


FIG. 4. Global section plots of oceanographic parameters under PI boundary conditions along the transect path indicated in Fig. S3. (a) Potential temperature and (b) its difference from the *World Ocean Atlas 2009* (WOA09; Levitus et al. 2010). (c) Salinity and (d) its difference from WOA09. (e) Ideal age, which is an artificial tracer that is reset to zero at the surface and increases elsewhere by 1 yr yr^{-1} . (f) Southern Ocean dye tracer that is restored to 100% at the surface south of 45°S and is diluted elsewhere only through water mass mixing.

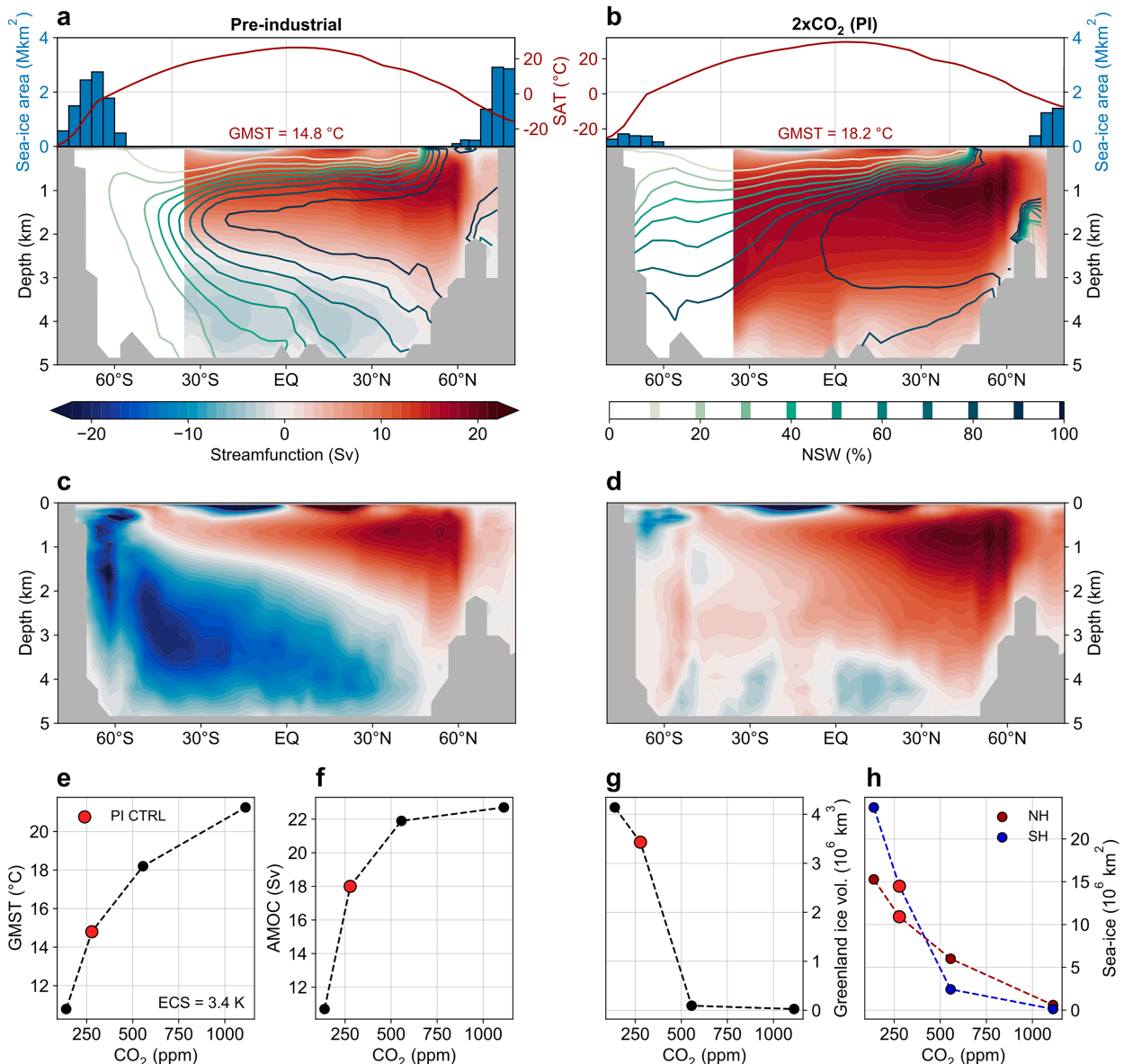


FIG. 5. Meridional distributions of surface atmospheric temperature (SAT) and sea ice extent, Atlantic streamfunction (filled contours), and northern-sourced water distribution (contour lines) for (a) the preindustrial (PI) and (b) a simulation with doubled CO₂ concentration relative to PI. Global streamfunction for (c) the preindustrial, and (d) doubled CO₂ concentrations. Also shown are CO₂ concentration vs (e) global mean surface temperature (GMST), (f) AMOC strength, (g) Greenland ice volume, and (h) sea ice extent for both hemispheres for sensitivity tests with 0.5, 2, and 4 times CO₂ concentrations relative to PI. The PI control run is marked as a filled red circle. All simulations are at steady state.

North Pacific is also well resolved, with the oldest water situated at middepths as Antarctic Bottom Water (AABW) is slowly mixed upward. The new parameterization of brine rejection stimulates more vigorous AABW compared to the previous version of the Bern3D model, which can be seen in the Atlantic distribution of the ventilation ages. However, as noted before NADW remains too shallow, and thus the deep North Atlantic is too old and bathed by too much AABW (Figs. 4e,f).

The preindustrial AMOC strength is 18 Sv and the zero iso-line of the streamfunction is at around 3 km water depth at

the equator (Fig. 5a) in good agreement with modern observations from the RAPID array (Frajka-Williams et al. 2019) (see Fig. S5 for Indo-Pacific and global MOC, and Fig. S6 for the barotropic streamfunction). In the deep Atlantic the anti-clockwise overturning circulation associated with AABW advection has a maximum of around 4 Sv, which is less than the 8 Sv AABW production today (Talley et al. 2003), but constitutes a major improvement compared to the previous Bern3D version where it was nearly absent. This is due to the improved parameterization of brine rejection that stimulates

increased AABW formation around Antarctica. The Antarctic Circumpolar Current has a strength of slightly more than 100 Sv calculated at the Drake Passage, and thus falls short of modern estimates that suggest a circulation strength of more than 140 Sv (Talley et al. 2003). The simulated Bering Strait throughflow, important for the freshwater balance of the Arctic and North Atlantic, is 1.2 Sv and hence in good agreement with observations that suggest a throughflow of 1.0 Sv (Woodgate 2018).

4. Sensitivities to changes in greenhouse gas concentrations

a. Abrupt CO₂ changes of 0.5, 2, and 4 times preindustrial

We first explore the sensitivities of the coupled model to abrupt changes in atmospheric CO₂ concentrations. After abruptly doubling CO₂ concentrations large fractions of sea ice are melted in both hemispheres, which is particularly pronounced in the Southern Hemisphere where less than 20% of the preindustrial sea ice area remains, and the Greenland ice sheet nearly fully disintegrates. In equilibrium the AMOC increases to a strength of 22 Sv, or 4 Sv stronger than the preindustrial control (Figs. 5b,f). At steady state after 50 000 model years the GMST is 18.2°C, which implies an equilibrium climate sensitivity of 3.4°C. Brine rejection around Antarctica is strongly reduced due to increased stratification in a warmer climate, and hence AABW formation nearly ceases and with it the lower circulation cell of the streamfunction. Consequently, the entire deep Atlantic is filled dominantly with northern-sourced water (Fig. 5b).

Four times preindustrial CO₂ concentration leads to a total GMST warming of about 6.7°C. The AMOC strength is about 22.5 Sv and thus only marginally stronger compared to the CO₂ doubling experiment. The Greenland ice sheet was already virtually gone for a CO₂ doubling, but for 4 times preindustrial CO₂ even the last remaining high-altitude glaciers are melted away in the southeastern Greenland mountain range (Fig. S7). Similarly, sea ice in both hemispheres entirely disappeared.

At an atmospheric CO₂ concentration of about 140 ppm (i.e., half the preindustrial) GMST is nearly 4°C colder at steady state compared to the preindustrial control. As we only simulate the Greenland ice sheet in these experiments, this excludes surface albedo feedbacks from the North American and Eurasian ice sheets. The Greenland ice sheet grows to a volume of $\sim 4.1 \times 10^6$ km³, about 20% larger than at preindustrial, which also appears to be the maximum ice volume Greenland can hold. Sea ice grows in both hemispheres, but to a larger extent in the Southern Hemisphere. This further enhances brine rejection around Antarctica and stimulates increased AABW formation. At the same time, NADW formation is weakened, which leads to a strongly reduced AMOC strength of ~ 10.5 Sv. This is close to the estimates of Atlantic overturning strength at the LGM (Pöppelmeier et al. 2023b), but we note that other glacial boundary conditions, such as increased wind stress due to the large continental ice sheets or enhanced diapycnal mixing as a

result of the lower sea level, which tend to increase AMOC (Pöppelmeier et al. 2021c), and increased dust content in the atmosphere reducing AMOC, are not considered in the experiment discussed here. A more complete glacial forcing is applied in the simulations presented in section 4.

b. Transient warming scenarios

Gradually increasing the CO₂ concentration by 0.5%, 1%, and 2% yr⁻¹ leads to an immediate and linear warming of the atmosphere [see section 2c(1) for details on the experiments]. The warming trends strongly decrease after the target CO₂ concentrations are reached, but warming still continues for at least ~ 2000 years afterward due to internal climate–ocean–ice feedbacks (Fig. 6a). For instance, the Greenland ice sheet starts melting lowering the land albedo. The initial melting of Greenland is slow, but accelerates after about 200 years, in particular for the simulations with quadrupled preindustrial CO₂ concentrations, and continues until virtually all ice is melted for all runs. The virtual ice-free state is reached after about 700 and 1500 years for the experiments with quadrupled and doubled CO₂, respectively. Sea ice responds rather quickly to the increase in atmospheric temperature (Figs. 6e,f). While a substantial fraction of sea ice remains for a doubling of CO₂ at the end of the simulations (in particular in the Northern Hemisphere), virtually all sea ice vanishes for a quadrupling of CO₂ within the first 1200 and 300 years for the Northern and Southern Hemisphere, respectively. Interestingly, a sudden second decrease in the Northern Hemisphere sea ice occurs after around 1900 years after the start of the simulation with a doubling of CO₂. This appears to be a direct response to a slight increase in GMST of 0.3°C at the same time and could be considered a regional tipping point.

The AMOC first decreases due to the freshwater addition from the melting sea ice, but then recovers after the sea ice extent somewhat stabilizes and continues to slowly increase for the rest of the experiment exceeding an overturning strength of 20 Sv after about 1000 years (Fig. 6b). Further, it appears that the multicentury-scale disintegration of the Greenland ice sheet represents only a minor perturbation to the AMOC. Due to the long response time of the deep ocean to atmospheric perturbations, MOT increases rather slowly and does not reach an equilibrium state for the CO₂ quadrupling experiments within the 2500 years of the simulations (Fig. 6d). The initial reduction but subsequent recovery of the AMOC is similar to the transient response of the AMOC to abrupt increases in CO₂ as simulated in coupled general circulation models as part of the LongRun Model Intercomparison Project (LongRunMIP; Bonan et al. 2022). However, while nearly all models of the LongRunMIP exhibit some AMOC recovery within the first 1000 years, only two models recover to a strength greater than their initial state as the Bern3D model does. Millennial-scale projections with an earlier Bern3D version found equilibrium AMOC strengths to be forcing dependent, with strengths larger than at preindustrial under low and vice versa under large radiative forcing (Battaglia and Joos 2018a). Moreover, a recent study performed with the NASA-GISS ModelE found that eight out of ten ensemble members

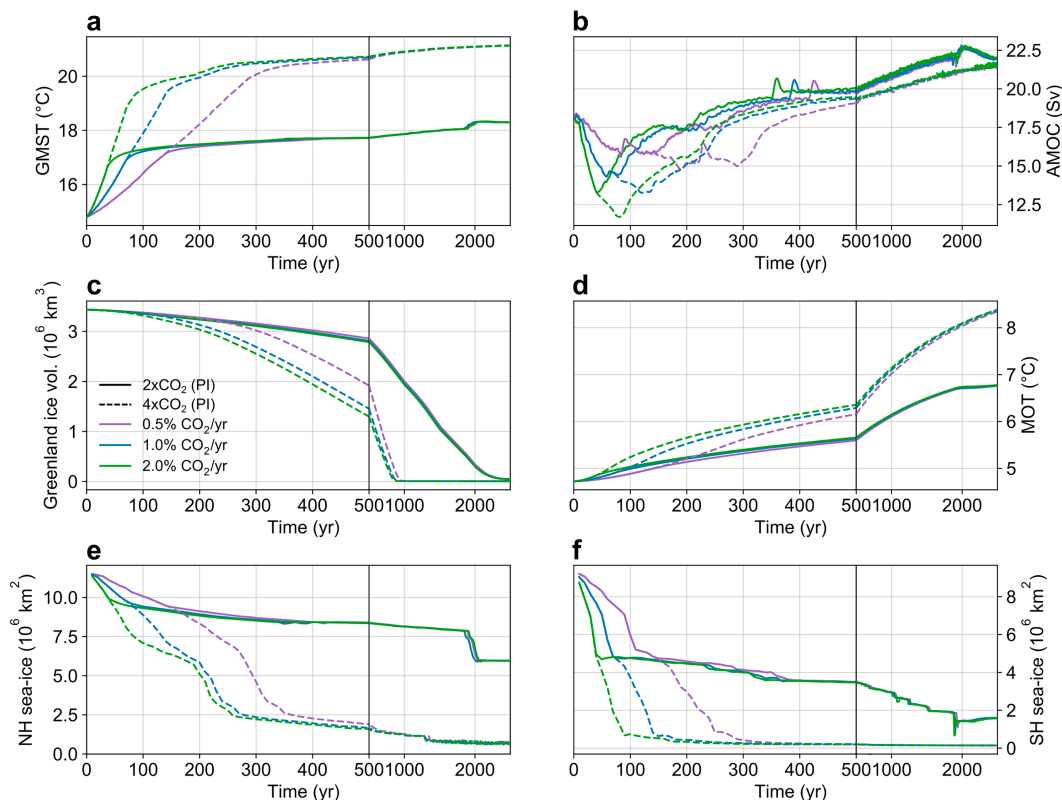


FIG. 6. Transient responses of (a) GMST, (b) AMOC strength (5-yr running mean), (c) Greenland ice volume, (d) MOT, (e) annual mean Northern Hemispheric sea ice area, and (f) annual mean Southern Hemispheric sea ice area to gradual CO_2 increases with a rate of 0.5% (purple), 1% (blue), and 2% (green) per year until either double (solid lines) or quadruple (dashed lines) the preindustrial CO_2 concentration is reached. After the target CO_2 concentration was reached (at years 140, 70, and 35 for doubling; at years 280, 140, and 70 for quadrupling), it was held constant until the end of the simulation. All other boundary conditions correspond to the preindustrial control.

also recover to a strong AMOC after an initial weakening as a response to the SSP2-4.5 scenario but two exhibit a bifurcation to a collapsed AMOC (Romanou et al. 2023).

5. Sensitivities to freshwater forcing

The AMOC plays a critical role for the interhemispheric transport of heat and carbon and is considered a tipping element in the global climate system (Stocker 2013) that is able to rapidly and irreversibly transition between multiple equilibrium states. We here therefore assess the AMOC hysteresis and general response to freshwater perturbations in the Bern3D model.

Perturbing the North Atlantic (45° – 70°N) freshwater balance by an increasing hosing flux slowly decreases the AMOC strength (Fig. 7a). This rather continuous weakening is interrupted by two rapid drops in AMOC strength at hosing fluxes of 0.12 and 0.24 Sv indicating nonlinear responses to the perturbations. Gradually reducing the hosing flux again reveals two distinct hysteresis loops, one with a width of about 0.08 Sv and a smaller one with 0.02 Sv. Reducing the rate of change of the hosing from 0.04 to 0.02 Sv kyr^{-1} only slightly modifies the hysteresis paths and reduces the widths, indicating that we are

able to accurately track the hysteresis diagram of the AMOC in the Bern3D model. This suggests that the AMOC exhibits not only two but three stable equilibrium states, the first at a strong AMOC, the second at around 10 Sv (see Fig. S8), and the final one at a collapsed state. However, when the freshwater forcing is removed the AMOC recovers to its initial strength (Fig. S8) suggesting that these transitions are fully reversible on millennial time scales. Under preindustrial boundary conditions the AMOC is monostable and relatively far away from the first tipping point.

The response of the AMOC to abrupt freshwater perturbations was examined by applying a hosing flux of 0.1–0.4 Sv to the North Atlantic over 500 years (Fig. 7b). For all experiments, the AMOC immediately weakens and then remains rather constant for the smallest hosing, but continues to decrease for stronger freshwater fluxes, such that freshwater fluxes of 0.3 and 0.4 Sv force the AMOC into its collapsed state. The weakening of about 5 Sv as a response to a hosing flux of 0.1 Sv is very similar to the multimodel mean response by Stouffer et al. (2006), which includes EMICs as well as more complex general circulation models. In general, the ocean response to freshwater hosing appears to be much alike between EMICs such as Bern3D and general circulation

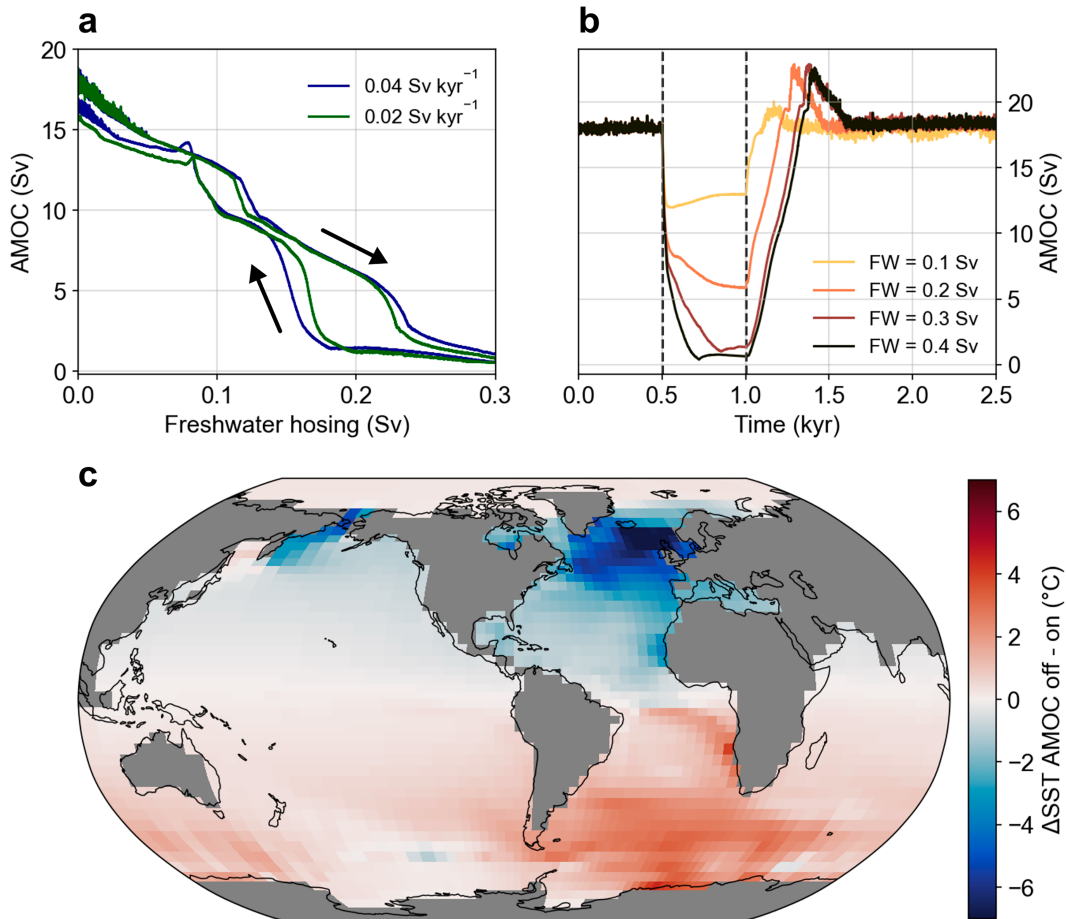


FIG. 7. (a) AMOC hysteresis with regard to freshwater hosing. Two different rates of change of the forcing were tested: 0.04 Sv kyr^{-1} (blue) and 0.02 Sv kyr^{-1} (green). (b) Response of the AMOC to transient freshwater (FW) perturbations between 0.1 and 0.4 Sv applied over 500 years (vertical dashed lines). (c) Global sea surface temperature (SST) difference between the AMOC's collapse [at the end of the hosing with 0.4 Sv in (b)] and control state.

models. Yet, atmospheric changes are smaller in Bern3D, mainly because of the simplified atmospheric dynamics. The recovery time scale in Bern3D is a linear function of the maximum AMOC reduction during the hosing period, but in all simulations it recovers within 500 years to its initial strength. When the AMOC is collapsed, meridional heat transport is strongly curtailed (Fig. S9), which manifests as the classical bipolar seesaw pattern (e.g., Stocker and Johnsen 2003) with strongly reduced SSTs of up to more than 7°C in the North Atlantic, particularly around Iceland, and warmer SSTs in the South Atlantic (Fig. 7c). Simulated changes in SST outside the Atlantic are rather small, but a modest cooling of around 4°C is also found at the Bering Sea, while somewhat warmer temperatures are found throughout the Indian Ocean and South Pacific.

6. Transient simulation of the last glacial cycle

a. Climate and ocean evolution

We transiently simulated the entire last glacial cycle with bidirectional coupling between the ice sheets and Earth

system model forced by the evolution of the orbital configuration and radiative forcing of greenhouse gases and aerosols (see section 2c for details; Figs. 8a–c). Both GMST and MOT evolve nearly congruently over the entire past 120 kyr and are characterized by gradual cooling that is interrupted by more rapid cooling at the beginning of Marine Isotope Stage (MIS) 4 and at the transition to the LGM (Figs. 8d,e), and are therefore in general agreement with the climate evolution of the last glacial cycle (Jouzel et al. 2007). Yet, MOT displays fewer high-frequency variations due to the large inertia of the deep ocean that attenuates temperature variations communicated from the atmosphere to the ocean. Recent reconstructions of MOT from the noble gas proxy measured from ancient air in polar ice cores suggest that during MIS4 MOT was as cold as during the LGM (Shackleton et al. 2021). Here we are unable to reproduce this with simulated MOT being about 0.5°C warmer during MIS4 compared to the LGM. Similarly, the model simulates temperature variations over Greenland and Antarctica (Figs. 9a,b) that are too small by a factor of about 2 compared to reconstructions (Kindler et al. 2014; Jouzel et al. 2007).

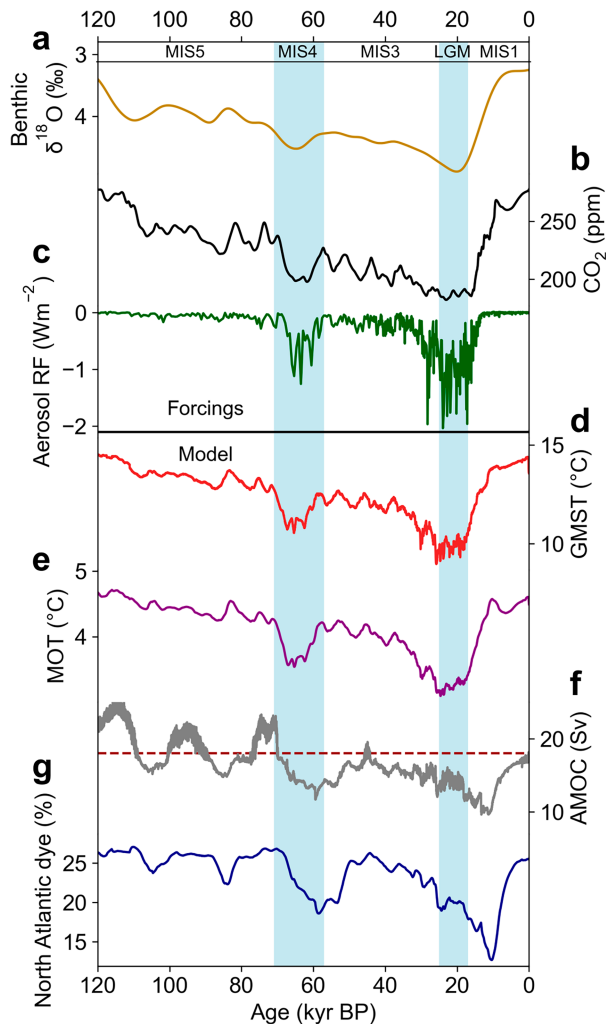


FIG. 8. Evolution of the model forcing: (a) benthic $\delta^{18}\text{O}$ stack (Lisiecki and Stern 2016) smoothed with a 10 kyr spline (used for wind stress and tidal mixing scaling; see section 2c for details), (b) atmospheric CO_2 concentrations (Köhler et al. 2017), and (c) aerosol radiative forcing as derived from the EDC dust record (Lambert et al. 2012; see section 2c for details). The model's response to the forcing: (d) global mean surface temperature (GMST), (e) mean ocean temperature (MOT), (f) AMOC strength (dashed red line marks preindustrial strength), and (g) global mean fraction of northern-sourced water as diagnosed by a North Atlantic dye that is restored to 100% between 46° and 76°N . Blue vertical bars mark the two major cold periods of MIS4 and the LGM. See Fig. 10 for the insolation forcing at 65°N .

The AMOC exhibits three large cycles with ~ 20 kyr period during MIS5 (Fig. 8f) that vary by up to 9 Sv in magnitude with a maximum AMOC strength of about 24 Sv (i.e., 6 Sv stronger than at preindustrial). These variations virtually disappear from MIS4 onward. The cause for this shift in AMOC variability is twofold. First, the waxing and waning of the continental ice sheets is heavily modulated by Northern Hemispheric summer insolation, which exhibits a strong contribution from precession (i.e., ~ 20 kyr period; Berger and

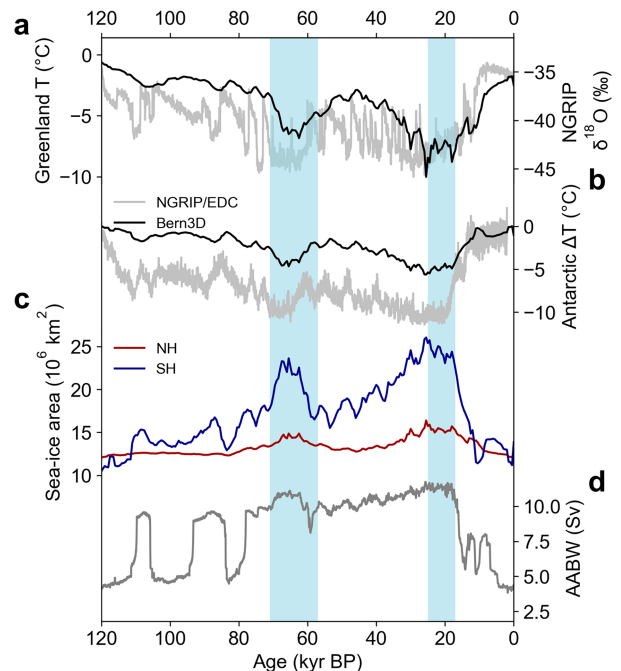


FIG. 9. Time series of simulated (a) Greenland and (b) Antarctic surface temperature as simulated by the Bern3D model (black) and reconstructed $\delta^{18}\text{O}$ from NGRIP (Andersen et al. 2004) and temperature from EPICA Dome C (EDC) ice cores (Jouzel et al. 2007). (c) Sea ice area of the Northern (red) and Southern (blue) Hemispheres. (d) Strength of Antarctic Bottom Water (AABW) in the Atlantic. Blue vertical shaded bars mark the time periods of MIS4 and the LGM.

Loutre 1991) and is most pronounced during MIS5 and weaker during MIS3 (Fig. 10d). During the ice sheet build-up phase net freshwater removal occurs, which drives the increase in AMOC. In contrast, when the ice sheets diminish meltwater directly enters the North Atlantic and weakens the AMOC (Fig. 10c). Second, from MIS4 onward the Southern Ocean sea ice extent (Fig. 9c) appears to have crossed a threshold that stimulates substantially stronger AABW formation (~ 10 vs 4 Sv at PI; Fig. 9d), which dampens the excursions to very vigorous AMOC states and limits the maximum AMOC strength to less than 20 Sv. Reconstructions of the AMOC from sedimentary Pa/Th show a similar first-order evolution over the past 120 kyr even though the precessional signal is not as pronounced in the data (Böhm et al. 2015). The reconstructed AMOC evolution is further interrupted by Heinrich events, which are not simulated in our setup, because of the missing fast flowing ice streams that lead to rapid calving events (see also section 2b). Interestingly, the northern-sourced water mass contribution never exceeds the modern fraction even during periods of stronger than modern AMOC during MIS5 (Fig. 8g). This decoupling of AMOC strength and water mass mixing could imply that proxies of water mass mixing may have difficulties accurately recording these strong AMOC events. For instance, reconstructions of neodymium and stable carbon isotopes display values comparable to the modern during the entire MIS5 (Hines et al. 2021;

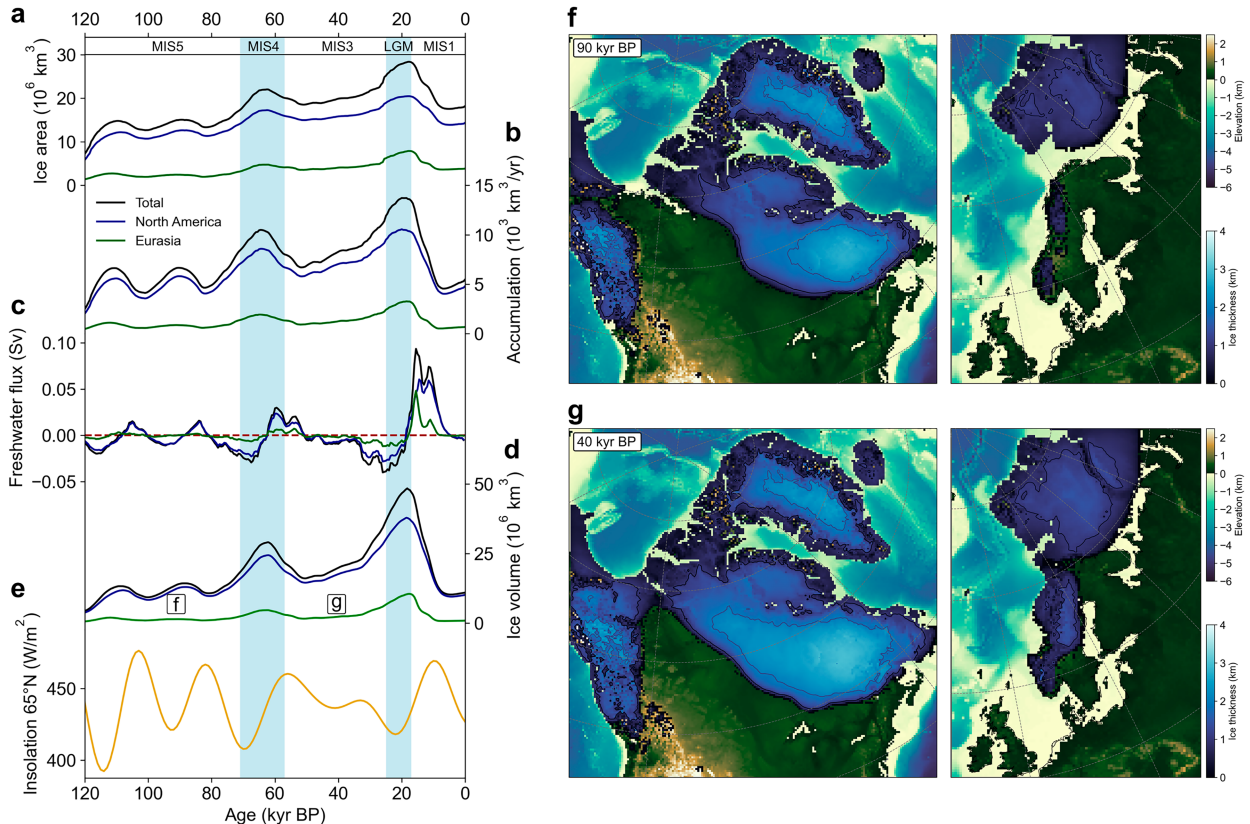


FIG. 10. Simulated evolution of (a) ice area, (b) accumulation rate, and (c) freshwater flux of the North American (blue) and Eurasian (green) ice sheets, and both combined (black). Note that freshwater removal is globally uniform while addition is only to the North Atlantic and Pacific. (d) Ice volume of the North American (blue) and Eurasian (green) ice sheets, and the total Northern Hemisphere (black). (e) Northern Hemisphere summer insolation at 65°N (Berger and Loutre 1991). Snapshots of ice thickness at (f) 90 and (g) 40 kyr BP for both ice sheets with contour lines every 1 km. External forcings of the simulation are depicted in Figs. 8a–c.

Pöppelmeier et al. 2021a), which could hence imply that either the AMOC strength was similar to today or that these proxies are insensitive to such changes. Yet notably, these proxy reconstructions exhibit very similar orbital-scale variations as simulated here with a North Atlantic dye tracer.

b. Ice sheet evolution

The simulated ice volume of the two Northern Hemispheric ice sheets (Fig. 9d) exhibits pronounced orbital-scale variations that mirror the evolution of the Northern Hemisphere summer insolation (Fig. 9g). The initial ice sheet buildup of the glacial inception shortly follows after the end of the last interglacial at 120 kyr BP. At around 110 and 90 kyr BP ice volume reaches two maxima during MIS5, which is followed by large ice sheet expansion during MIS4. During this first half of the glacial cycle ice sheet growth and decay are mainly focused on the Cordilleran, Arctic Archipelago, and Labrador regions in North America and the Barents Sea and Fennoscandia in Eurasia (Figs. S10 and S11). The Cordilleran and Laurentide ice sheets first start merging during MIS4 but separate again at around 50 kyr BP before fully merging only prior to the LGM. Compared to reconstructions of global mean sea level from benthic $\delta^{18}\text{O}$ (Waelbroeck et al. 2002)

and ICE-6G (Peltier et al. 2015) total ice volume simulated with the Bern3D model is underestimated throughout most of the last glacial cycle except for the LGM (Fig. 11). Note however that both reconstructions include sea level change from variations of the Antarctic ice sheet as well, which are not considered here. Since the contribution from Antarctica to global sea level change is estimated at less than 20 m at the LGM ($\sim 8 \times 10^6 \text{ km}^3$) (Huybrechts 2002; Pittard et al. 2022), this effect cannot account for the observed difference. The deviation from these two reconstructions is largest during MIS3 with an underestimation of up to 40 m. Yet, more recent studies that focus on MIS3 indicate that sea level was in fact much shallower than these initial reconstructions suggested (e.g., Farmer et al. 2023; Pico et al. 2016; Gowan et al. 2021) and are more in line with the ice volume simulated here. For instance, simulated total ice volume more than doubles from MIS3 to the LGM, in agreement with reconstructions that indicate the closing of the Bering Strait (sill depth of -53 m) only at around 36 kyr BP (Farmer et al. 2023). Although the initial disintegration of the ice sheets during the last deglaciation is simulated in good agreement with reconstructions, residual ice sheets in both North America and Eurasia do not fully vanish during the Holocene with around $8 \times 10^6 \text{ km}^3$ (or

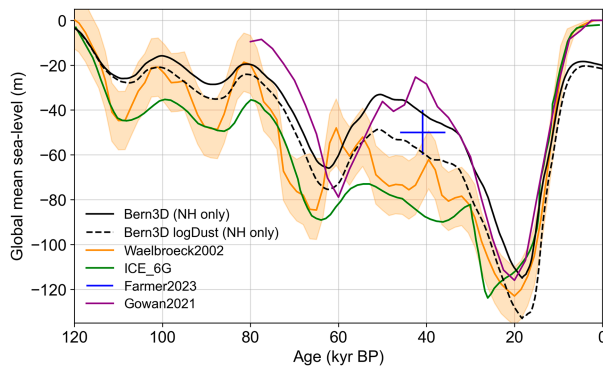


FIG. 11. Global mean sea level as simulated by the Bern3D model (black dashed line is with logarithmic dust scaling for the additional radiative forcing as depicted in Fig. S11) compared to reconstructions inferred from global mean benthic $\delta^{18}\text{O}$ stack (orange; Waelbroeck et al. 2002), glacial isostatic adjustment of ICE-6G (green; Peltier et al. 2015), the timing of the opening of the Bering Strait (blue; Farmer et al. 2023), and geological constraints (Gowan et al. 2021). Note that only the Northern Hemispheric ice sheets are simulated by the Bern3D model while reconstructions consider also changes in the Antarctic ice sheet.

~ 20 m of sea level equivalent) left at the end of the simulation. Note, however, that we here focused on simulating LGM ice sheets in good agreement with reconstructions and only to a lesser extent on a realistic deglaciation.

Continental ice area extent shows attenuated variability over the last glacial cycle compared to ice volume (Fig. 10a) implying that ice thickness also substantially varies on these orbital time scales. Further, ice accumulation (Fig. 10b) peaks slightly (~ 2 kyr) before the maximum ice volume is reached during precessional cycles, since it is a function of both climate and ice area extent. The freshwater fluxes associated with the growth and decay of the ice sheets are generally small (< 0.02 Sv) during the entire last glacial cycle (Fig. 10c), which is a result of the simplified ice physics that are unable to accurately simulate ice sheet/shelf instabilities that are thought to have caused past Heinrich events (Broecker 1994). Only during the last deglaciation model freshwater fluxes reach up to 0.1 Sv, yet the large meltwater pulses of ~ 0.3 Sv (e.g., Liu et al. 2016) that characterized the deglaciation are not simulated.

c. Ice sheet sensitivity

To explore and illustrate the sensitivities of the ice sheet model to critical parameters and forcing, we performed a number of experiments. In a first sensitivity experiment, we changed the time scale of the relaxing mantle from 2 to 10 kyr, which impacts how quickly the bed topography adjusts to changes in ice load. Similar to previous modeling efforts (Ganopolski et al. 2010; Gregoire et al. 2012), we find only little change in the ice sheet evolution depending on the mantle relaxation time scale (Fig. S10). Even though this process is thought to play an important role for the ice–elevation feedback (Levermann and Winkelmann 2016), it appears to have

little effect on multimillennial-scale ice sheet evolution during the last glacial cycle.

Many ice sheet models employ a so-called flow enhancement factor, which is a coefficient in the flow law (Paterson 1994) that increases ice velocities. Here we test the effect of reducing this factor from 5.5 in the control simulation to 2.0. We find a weak sensitivity of the ice sheet model on this parameter, with virtually no difference in ice volume throughout most of the last glacial cycle (Fig. S10). The only exception is during MIS3 when the ice volume of both the North American and Eurasian ice sheets decreases less than for the control simulation. Because of the lower velocities, the ice advances more slowly to regions of high ablation and ice thickness hence decreases slower.

Finally, we performed an experiment for which we modified the aerosol radiative forcing to be logarithmically scaled from the EPICA Dome C dust record (not linearly as in the control run) (Köhler et al. 2010). This forcing leads to lower temperatures mostly during MIS5 and MIS3 on the order of $0.4^{\circ}\text{--}0.7^{\circ}\text{C}$ in GMST (Fig. S11). We find that the total ice volume responds rather linearly to the colder temperatures on these multimillennial time scales with an increase of about $1 \times 10^6 \text{ km}^3$ per 0.1°C cooling. As such, the maximum additional ice volume is about $7 \times 10^6 \text{ km}^3$ (or 18 m additional lower sea level; Fig. 11) at around 50 kyr BP. This increased ice volume reduces the bias relative to sea level reconstructions based on ICE-6G (Peltier et al. 2015) and derived from benthic $\delta^{18}\text{O}$ (Waelbroeck et al. 2002) by about 50%, yet discrepancies to these earlier reconstructions remain in particular during MIS5. More recent sea level reconstructions (Gowan et al. 2021; Farmer et al. 2023) generally agree better with the simulated sea level evolution. This suggests that further sea level constraints are required in order to better judge the performance of the model, as the reconstructions diverge by more than 40 m during MIS3.

7. Climate, ocean, and ice sheets at the LGM

We evaluate the LGM state (20 kyr BP) of the standard transient simulation of the last glacial cycle described in section 6 (i.e., linear dust scaling for the aerosol forcing, and ice sheet parameters as in Table S2). The simulated GMST is 9.9°C or about 5°C colder than during PI, which is at the warmer end of recent estimates that indicate GMST anomalies ranging between -4.5° and -7.1°C (Annan et al. 2022; Osman et al. 2021; Tierney et al. 2020). The strongest cooling is concentrated at the northern high latitudes, due to the elevation effect of the continental ice sheets (Figs. 12a,d) with zonal mean cooling exceeding 10°C . Enhanced cooling is also simulated at the southern high latitudes, albeit to a lesser degree compared to the northern latitudes, and is instead caused by the expansion of sea ice in the Southern Ocean (Figs. 12b,e).

The MOT anomaly relative to PI is 1.6°C and thus falls short of the 2.6°C reconstructed with the noble gas thermometry from ancient air trapped in polar ice (Bereiter et al. 2018) but agrees within uncertainties with a recent reassessment of the inferred MOT from noble gases (Pöppelmeier et al. 2023a).

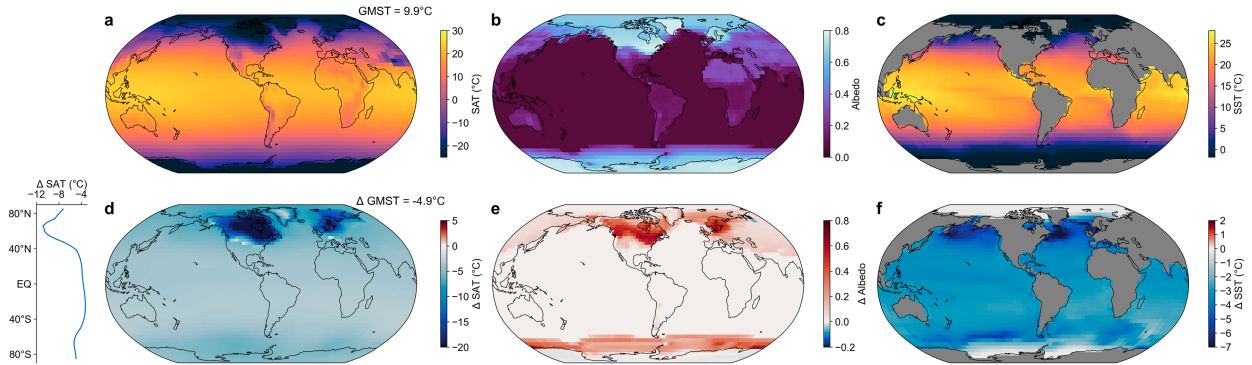


FIG. 12. (a)–(c) Surface atmospheric temperature (SAT), albedo, and sea surface temperature (SST) at the LGM and (d)–(f) their anomalies relative to the preindustrial control simulation. Global mean surface temperature (GMST) at the LGM is 9.9°C, and thus 4.9°C colder than the preindustrial.

The ensemble mean of the MOT anomaly simulated with more complex models in the Paleo Model Intercomparison Project 3 is also 1.6°C (Bereiter et al. 2018), the same as simulated here, highlighting systematic model–data discrepancies that require more in-depth investigations in the future. In contrast, simulated global mean SST is 2.9°C colder at the LGM compared to PI, in good agreement with reconstructions that suggest a cooling of $3.1^{\circ} \pm 0.3^{\circ}\text{C}$ (Tierney et al. 2020). Enhanced sea surface cooling is found here in the northern high latitudes, in particular the subpolar North Atlantic (Figs. 12c,f). This pattern is a result of the bipolar seesaw of the weakened AMOC during the LGM (cf. Fig. 7c), which is decreased by about 4 to 14 Sv (Figs. 13a,b). A recent constraint of the LGM AMOC strength from a model–data comparison indicates a weakening of about one-third relative to PI (Pöppelmeier et al. 2023b) and is thus only slightly weaker to the here simulated decrease of $\sim 20\%$. As during MIS3 and MIS4, AABW formation is strongly enhanced at the LGM (Fig. 9), because Southern Ocean sea ice extent is at its maximum stimulating vigorous brine rejection and hence deep water formation. On the other hand, reconstructions from the Weddell Sea suggest no or very limited export of bottom waters during the LGM (Huang et al. 2020), but open ocean convection cannot yet be excluded, which is the dominant process for deep water formation in the model.

Both simulated ice sheets are not fully in equilibrium at the LGM, underlining that a transient “spinup” of simulating the entire last glacial cycle is indeed necessary for a fair model–data comparison (Figs. S12 and S13). The maximum ice volumes of 36.9×10^6 and $9.7 \times 10^6 \text{ km}^3$ for the North American and Eurasian ice sheets, respectively (Figs. 13c,d), are reached between 20 and 19 kyr BP. These compare fairly well to the ICE-6G reconstructions of 35.1×10^6 and $6.7 \times 10^6 \text{ km}^3$, respectively, even though the Eurasian ice sheet volume is overestimated here by about 40%. Biases of the North American ice sheet form a spatial dipole pattern, where ice thickness is underestimated at the Arctic Archipelago and east of the Rocky Mountains while it is increasingly overestimated east of $\sim 90^{\circ}\text{W}$ (Fig. S14). In addition, Alaska is glaciated too strongly, which reconstructions suggest was ice free during

the LGM (Peltier et al. 2015). The simulated Eurasian ice sheet extends too far into Siberia and its thickness is strongly overestimated over the Baltic Sea and North Sea (Fig. S15). Presumably, the too thick ice sheet over regions that exhibit very soft bed conditions of marine sediments is caused by the simplified parameterization of basal friction employed here that does not differentiate between compacted and loose sediments.

In summary, we here demonstrated that the coupled Bern3D ice sheet model is able to realistically simulate the entire last glacial cycle cumulating in an LGM state that compares well to reconstructions of climate, ocean, and ice characteristics, even though some aspects of the last deglaciation are not simulated in full agreement with reconstructions.

8. Conclusions

We here presented a new version of the Bern3D EMIC that incorporates a higher resolved spatial grid, new parameterizations of diapycnal diffusivity and brine rejection, and the option for bidirectionally coupling it to the glimmer-CISM ice sheet model. The model simulates the preindustrial climate well, but biases persist in precipitation and evaporation due to the simplified atmosphere module that further imprint in sea surface temperature and salinity. As a result of the relatively coarse spatial resolution of the model, ocean eddies cannot be resolved and are instead parameterized as diffusive processes. This, however, comes with the advantage that the model is computationally very inexpensive and able to simulate ~ 10 kyr per day in its fully coupled mode. We further performed a number of sensitivity tests that characterize the model’s response to abrupt perturbations such as atmospheric CO_2 changes and North Atlantic freshwater hosing. These experiments demonstrate that the Bern3D v3.0 model performs similarly to state-of-the-art climate models in many parameters and exhibits an equilibrium climate sensitivity of 3.4°C.

To test the climate–ocean–ice interactions of the coupled model, we simulated the entire last glacial cycle with interactive North American and Eurasian ice sheets. In the simulation, ice sheets first start forming immediately after the last interglacial and exhibit pronounced variability on orbital

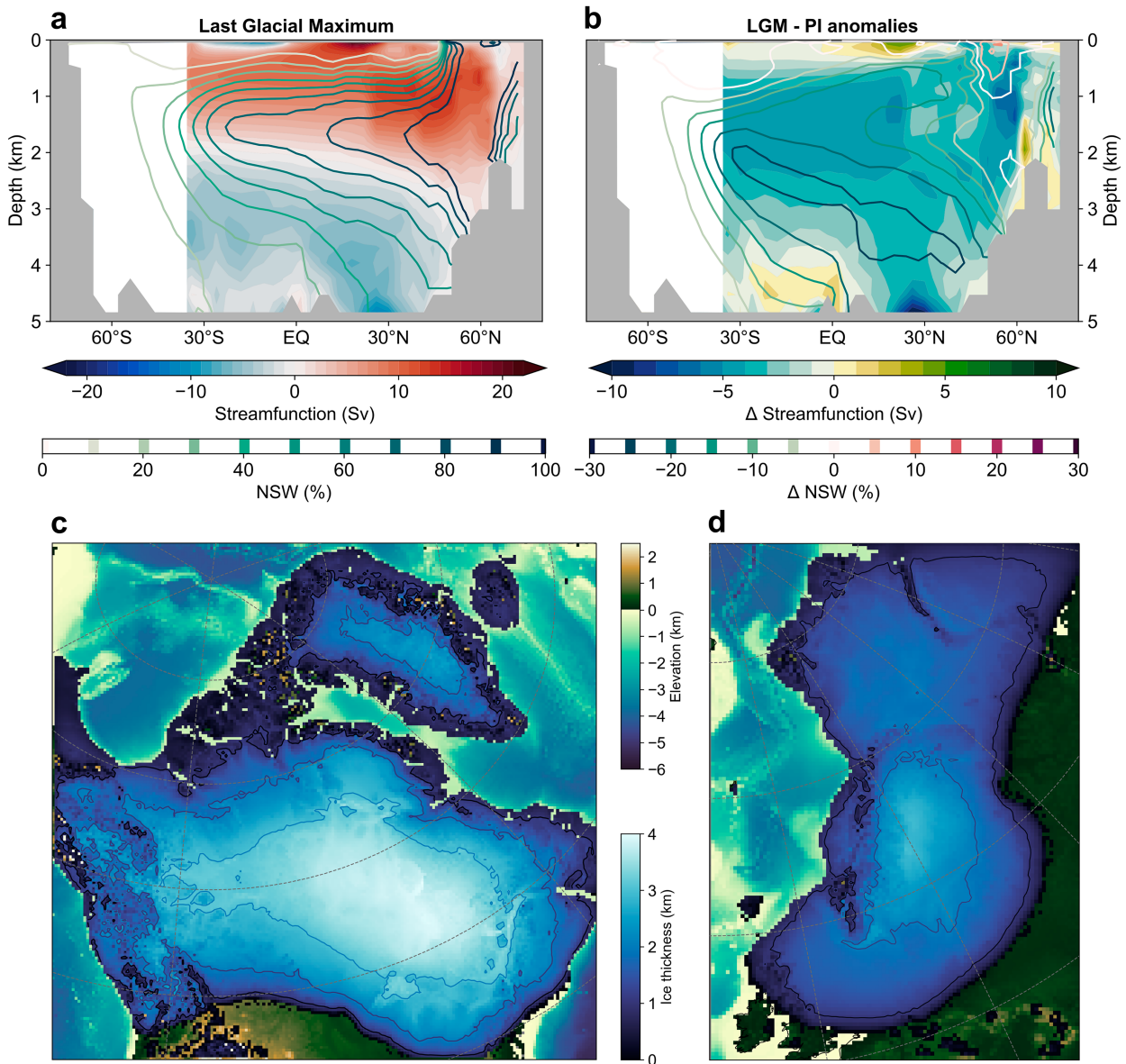


FIG. 13. (a) Atlantic streamfunction (filled contours) and northern-sourced water (NSW) distribution (contour lines) of the LGM. (b) Anomalies of the LGM Atlantic streamfunction and NSW distribution relative to the PI control simulation (Fig. 5a). (c) North American and (d) Eurasian ice sheet thickness at the LGM (contour lines every 1 km).

(mainly precessional) time scale throughout the last glacial cycle. Overall, ice volume is simulated in reasonable agreement with reconstructions of past sea level and the ice extent and volume at the LGM agrees well with the ICE-6G reconstruction. Dansgaard-Oeschger and Heinrich events, which characterized millennial-scale variability of the last glacial, are not simulated with the current setup, but might emerge when enabling higher-order ice physics that are readily available, albeit at a significant increase in computational cost. Further, improvements could come from coupling a surface energy-mass balance model, such as the Bergen Snow Simulator (BESSI; Born et al. 2019), to the Bern3D model to directly drive the ice sheet model with the surface mass balance. For

simulating multiple glacial-interglacial cycles this approach, however, is currently computationally too expensive. At the LGM, the climate and ocean state are simulated in good agreement with most reconstructions exhibiting features such as pronounced Northern Hemispheric cooling and a shallow and weak AMOC.

The high computational efficiency of the coupled Bern3D model makes it ideally suited for simulations of multimillennial to glacial-interglacial time scales and the investigation of interaction and sensitivities of the ocean-atmosphere-ice system on these time scales. Yet, it should be also noted that the high computational efficiency comes at the cost of more simplifications and parameterizations of processes, and the model

can hence not simulate interannual climate variability such as El Niño–Southern Oscillation or the North Atlantic Oscillation. Large ensemble simulations, for instance, to explore the impact and ultimately to constrain uncertain parameters are another possible application of the Bern3D model. In the future, we will further exploit the rich palette of ocean tracers implemented in the model for comprehensive model–roxy evaluations and innovative proxy interpretations to better constrain past climate states that can complement more complex model approaches. Finally, the Bern3D v3.0 model is now ready to simulate glacial–interglacial cycles including a coupled dynamical carbon cycle model consisting of land and marine biospheres, as well as a palette of biogeochemical and physical tracers. This will be presented in a forthcoming study.

Acknowledgments. This study was supported by the European Union’s Horizon 2020 research and innovation program under Grant Agreements 101023443 (project CliMoTran) to FP and 820970 (project TiPES) to TFS. The work reflects only the authors’ view; the European Commission and their executive agency are not responsible for any use that may be made of the information the work contains. TFS and FJ are further supported by the Swiss National Science Foundation (Grants 200020_200492 and 200020_200511, respectively). Calculations were performed on UBELIX, the high-performance computing cluster at the University of Bern. We thank Gunnar Jansen for technical support and Andreas Born, Christian Wirths, and Johannes Sutter for fruitful discussions on the ice sheet coupling.

Data availability statement. The Bern3D model output is publicly available at the Zenodo repository (<https://doi.org/10.5281/zenodo.8176754>).

REFERENCES

- Andersen, K. K., and Coauthors, 2004: High-resolution record of Northern Hemisphere climate extending into the last interglacial period. *Nature*, **431**, 147–151, <https://doi.org/10.1038/nature02805>.
- Annan, J. D., J. C. Hargreaves, and T. Mauritsen, 2022: A new global surface temperature reconstruction for the Last Glacial Maximum. *Climate Past*, **18**, 1883–1896, <https://doi.org/10.5194/cp-18-1883-2022>.
- Bartlein, P. J., and Coauthors, 2011: Pollen-based continental climate reconstructions at 6 and 21 ka: A global synthesis. *Climate Dyn.*, **37**, 775–802, <https://doi.org/10.1007/s00382-010-0904-1>.
- Battaglia, G., and F. Joos, 2018a: Hazards of decreasing marine oxygen: The near-term and millennial-scale benefits of meeting the Paris climate targets. *Earth Syst. Dyn.*, **9**, 797–816, <https://doi.org/10.5194/esd-9-797-2018>.
- , and —, 2018b: Marine N₂O emissions from nitrification and denitrification constrained by modern observations and projected in multimillennial global warming simulations. *Global Biogeochem. Cycles*, **32**, 92–121, <https://doi.org/10.1002/2017GB005671>.
- , M. Steinacher, and F. Joos, 2016: A probabilistic assessment of calcium carbonate export and dissolution in the modern ocean. *Biogeosciences*, **13**, 2823–2848, <https://doi.org/10.5194/bg-13-2823-2016>.
- Bauer, E., and A. Ganopolski, 2017: Comparison of surface mass balance of ice sheets simulated by positive-degree-day method and energy balance approach. *Climate Past*, **13**, 819–832, <https://doi.org/10.5194/cp-13-819-2017>.
- Bereiter, B., S. Shackleton, D. Baggenstos, K. Kawamura, and J. Severinghaus, 2018: Mean global ocean temperatures during the last glacial transition. *Nature*, **553**, 39–44, <https://doi.org/10.1038/nature25152>.
- Berger, A. L., 1978: Long-term variations of daily insolation and quaternary climatic changes. *J. Atmos. Sci.*, **35**, 2362–2367, [https://doi.org/10.1175/1520-0469\(1978\)035<2362:LTVODI>2.0.CO;2](https://doi.org/10.1175/1520-0469(1978)035<2362:LTVODI>2.0.CO;2).
- , and M. F. Loutre, 1991: Insolation values for the climate of the last 10 million years. *Quat. Sci. Rev.*, **10**, 297–317, [https://doi.org/10.1016/0277-3791\(91\)90033-Q](https://doi.org/10.1016/0277-3791(91)90033-Q).
- Böhm, E., and Coauthors, 2015: Strong and deep Atlantic meridional overturning circulation during the last glacial cycle. *Nature*, **517**, 73–76, <https://doi.org/10.1038/nature14059>.
- Bonan, D. B., A. F. Thompson, E. R. Newsom, S. Sun, and M. Rugenstein, 2022: Transient and equilibrium responses of the Atlantic overturning circulation to warming in coupled climate models: The role of temperature and salinity. *J. Climate*, **35**, 5173–5193, <https://doi.org/10.1175/JCLI-D-21-0912.1>.
- Born, A., M. A. Imhof, and T. F. Stocker, 2019: An efficient surface energy-mass balance model for snow and ice. *Cryosphere*, **13**, 1529–1546, <https://doi.org/10.5194/tc-13-1529-2019>.
- Broecker, W. S., 1994: Massive iceberg discharges as triggers for global climate change. *Nature*, **372**, 421–424, <https://doi.org/10.1038/372421a0>.
- Choudhury, D., A. Timmermann, F. Schloesser, M. Heinemann, and D. Pollard, 2020: Simulating marine isotope stage 7 with a coupled climate–ice sheet model. *Climate Past*, **16**, 2183–2201, <https://doi.org/10.5194/cp-16-2183-2020>.
- Claussen, M., and Coauthors, 2002: Earth system models of intermediate complexity: Closing the gap in the spectrum of climate system models. *Climate Dyn.*, **18**, 579–586, <https://doi.org/10.1007/s00382-001-0200-1>.
- Dinauer, A., F. Adolphi, and F. Joos, 2020: Mysteriously high $\Delta^{14}\text{C}$ of the glacial atmosphere: Influence of ^{14}C production and carbon cycle changes. *Climate Past*, **16**, 1159–1185, <https://doi.org/10.5194/cp-16-1159-2020>.
- Edwards, N. R., A. J. Willmott, and P. D. Killworth, 1998: On the role of topography and wind stress on the stability of the thermohaline circulation. *J. Phys. Oceanogr.*, **28**, 756–778, [https://doi.org/10.1175/1520-0485\(1998\)028<0756:OTROTA>2.0.CO;2](https://doi.org/10.1175/1520-0485(1998)028<0756:OTROTA>2.0.CO;2).
- Farmer, J. R., and Coauthors, 2023: The Bering Strait was flooded 10,000 years before the last glacial maximum. *Proc. Natl. Acad. Sci. USA*, **120**, e2206742119, <https://doi.org/10.1073/pnas.2206742119>.
- Frajka-Williams, E., and Coauthors, 2019: Atlantic meridional overturning circulation: Observed transport and variability. *Front. Mar. Sci.*, **6**, 260, <https://doi.org/10.3389/fmars.2019.00260>.
- Fyke, J. G., A. J. Weaver, D. Pollard, M. Eby, L. Carter, and A. MacKintosh, 2011: A new coupled ice sheet/climate model: Description and sensitivity to model physics under Eemian, Last Glacial Maximum, late Holocene and modern climate conditions. *Geosci. Model Dev.*, **4**, 117–136, <https://doi.org/10.5194/gmd-4-117-2011>.

- Ganopolski, A., and V. Brovkin, 2017: Simulation of climate, ice sheets and CO₂ evolution during the last four glacial cycles with an Earth system model of intermediate complexity. *Climate Past*, **13**, 1695–1716, <https://doi.org/10.5194/cp-13-1695-2017>.
- , R. Calov, and M. Claussen, 2010: Simulation of the last glacial cycle with a coupled climate ice-sheet model of intermediate complexity. *Climate Past*, **6**, 229–244, <https://doi.org/10.5194/cp-6-229-2010>.
- Gowan, E. J., and Coauthors, 2021: A new global ice sheet reconstruction for the past 80 000 years. *Nat. Commun.*, **12**, 1199, <https://doi.org/10.1038/s41467-021-21469-w>.
- Gregoire, L. J., A. J. Payne, and P. J. Valdes, 2012: Deglacial rapid sea level rises caused by ice-sheet saddle collapses. *Nature*, **487**, 219–222, <https://doi.org/10.1038/nature11257>.
- Gregory, J. M., O. J. H. Browne, A. J. Payne, J. K. Ridley, and I. C. Rutt, 2012: Modelling large-scale ice-sheet–climate interactions following glacial inception. *Climate Past*, **8**, 1565–1580, <https://doi.org/10.5194/cp-8-1565-2012>.
- Griffies, S. M., 1998: The Gent–McWilliams skew flux. *J. Phys. Oceanogr.*, **28**, 831–841, [https://doi.org/10.1175/1520-0485\(1998\)028<0831:TGMSF>2.0.CO;2](https://doi.org/10.1175/1520-0485(1998)028<0831:TGMSF>2.0.CO;2).
- Heinemann, M., A. Timmermann, O. E. Timm, F. Saito, and A. Abe-Ouchi, 2014: Deglacial ice sheet meltdown: Orbital pacemaking and CO₂ effects. *Climate Past*, **10**, 1567–1579, <https://doi.org/10.5194/cp-10-1567-2014>.
- Hines, S. K. V., L. Bolge, S. L. Goldstein, C. D. Charles, I. R. Hall, and S. R. Hemming, 2021: Little change in ice age water mass structure from Cape Basin benthic neodymium and carbon isotopes. *Paleoceanogr. Paleoclimatol.*, **36**, e2021PA004281, <https://doi.org/10.1029/2021PA004281>.
- Holden, P. B., N. R. Edwards, K. Fraedrich, E. Kirk, F. Lunkeit, and X. Zhu, 2016: PLASIM-GENIE v1.0: A new intermediate complexity AOGCM. *Geosci. Model Dev.*, **9**, 3347–3361, <https://doi.org/10.5194/gmd-9-3347-2016>.
- Huang, H., M. Gutjahr, A. Eisenhauer, and G. Kuhn, 2020: No detectable Weddell Sea Antarctic bottom water export during the last and penultimate glacial maximum. *Nat. Commun.*, **11**, 424, <https://doi.org/10.1038/s41467-020-14302-3>.
- Huybrechts, P., 2002: Sea-level changes at the LGM from ice-dynamic reconstructions of the Greenland and Antarctic ice sheets during the glacial cycles. *Quat. Sci. Rev.*, **21**, 203–231, [https://doi.org/10.1016/S0277-3791\(01\)00082-8](https://doi.org/10.1016/S0277-3791(01)00082-8).
- IPCC, 2021: *Climate Change 2021: The Physical Science Basis*. Cambridge University Press, 2391 pp., <https://doi.org/10.1017/9781009157896>.
- Jeltsch-Thömmes, A., and F. Joos, 2023: Carbon cycle responses to changes in weathering and the long-term fate of stable carbon isotopes. *Paleoceanogr. Paleoclimatol.*, **38**, e2022PA004577, <https://doi.org/10.1029/2022PA004577>.
- , G. Battaglia, O. Cartapanis, S. L. Jaccard, and F. Joos, 2019: Low terrestrial carbon storage at the last glacial maximum: Constraints from multi-proxy data. *Climate Past*, **15**, 849–879, <https://doi.org/10.5194/cp-15-849-2019>.
- , T. F. Stocker, and F. Joos, 2020: Hysteresis of the Earth system under positive and negative CO₂ emissions. *Environ. Res. Lett.*, **15**, 124026, <https://doi.org/10.1088/1748-9326/abc4af>.
- Joughin, I., B. E. Smith, I. M. Howat, T. Scambos, and T. Moon, 2010: Greenland flow variability from ice-sheet-wide velocity mapping. *J. Glaciol.*, **56**, 415–430, <https://doi.org/10.3189/002214310792447734>.
- Jouzel, J., and Coauthors, 2007: Orbital and millennial Antarctic climate variability over the past 800,000 years. *Science*, **317**, 793–796, <https://doi.org/10.1126/science.1141038>.
- Kalnay, E., and Coauthors, 1996: The NCEP NCAR 40-Year Reanalysis Project. *Bull. Amer. Meteor. Soc.*, **77**, 437–472, [https://doi.org/10.1175/1520-0477\(1996\)077<0437:TNYRP>2.0.CO;2](https://doi.org/10.1175/1520-0477(1996)077<0437:TNYRP>2.0.CO;2).
- Kindler, P., M. Guillevic, M. Baumgartner, J. Schwander, A. Landais, and M. Leuenberger, 2014: Temperature reconstruction from 10 to 120 kyr b2k from the NGRIP ice core. *Climate Past*, **10**, 887–902, <https://doi.org/10.5194/cp-10-887-2014>.
- Köhler, P., R. Bintanja, H. Fischer, F. Joos, R. Knutti, G. Lohmann, and V. Masson-Delmotte, 2010: What caused Earth's temperature variations during the last 800,000 years? Data-based evidence on radiative forcing and constraints on climate sensitivity. *Quat. Sci. Rev.*, **29**, 129–145, <https://doi.org/10.1016/j.quascirev.2009.09.026>.
- , C. Nehrbass-Ahles, J. Schmitt, T. F. Stocker, and H. Fischer, 2017: A 156 kyr smoothed history of the atmospheric greenhouse gases CO₂, CH₄, and N₂O and their radiative forcing. *Earth Syst. Sci. Data*, **9**, 363–387, <https://doi.org/10.5194/essd-9-363-2017>.
- Lambeck, K., and J. Chappell, 2001: Sea level change through the last glacial cycle. *Science*, **292**, 679–686, <https://doi.org/10.1126/science.1059549>.
- Lambert, F., M. Bigler, J. P. Steffensen, M. Hutterli, and H. Fischer, 2012: Centennial mineral dust variability in high-resolution ice core data from Dome C, Antarctica. *Climate Past*, **8**, 609–623, <https://doi.org/10.5194/cp-8-609-2012>.
- Laske, G., and G. Masters, 1997: A global digital map of sediment thickness. *Eos, Trans. Amer. Geophys. Union*, **78**, F483.
- Levermann, A., and R. Winkelmann, 2016: A simple equation for the melt elevation feedback of ice sheets. *Cryosphere*, **10**, 1799–1807, <https://doi.org/10.5194/tc-10-1799-2016>.
- Levitus, S., and Coauthors, 2010: *Temperature*. Vol. 1, *World Ocean Atlas 2009*, NOAA Atlas NESDIS 68, 196 pp., <https://repository.library.noaa.gov/view/noaa/1259>.
- Lienert, S., and F. Joos, 2018: A Bayesian ensemble data assimilation to constrain model parameters and land-use carbon emissions. *Biogeosciences*, **15**, 2909–2930, <https://doi.org/10.5194/bg-15-2909-2018>.
- Lipscomb, W. H., and Coauthors, 2019: Description and evaluation of the Community Ice Sheet Model (CISM) v2.1. *Geosci. Model Dev.*, **12**, 387–424, <https://doi.org/10.5194/gmd-12-387-2019>.
- Lisiecki, L. E., and J. V. Stern, 2016: Regional and global benthic $\delta^{18}\text{O}$ stacks for the last glacial cycle. *Paleoceanogr. Paleoclimatol.*, **31**, 1368–1394, <https://doi.org/10.1002/2016PA003002>.
- Liu, J., G. A. Milne, R. E. Kopp, P. U. Clark, and I. Shennan, 2016: Sea-level constraints on the amplitude and source distribution of Meltwater Pulse 1A. *Nat. Geosci.*, **9**, 130–134, <https://doi.org/10.1038/ngeo2616>.
- Menviel, L., F. Joos, and S. P. Ritz, 2012: Simulating atmospheric CO₂, ¹³C and the marine carbon cycle during the last glacial-interglacial cycle: Possible role for a deepening of the mean remineralization depth and an increase in the oceanic nutrient inventory. *Quat. Sci. Rev.*, **56**, 46–68, <https://doi.org/10.1016/j.quascirev.2012.09.012>.
- Morlighem, M., E. Rignot, J. Mouginot, H. Seroussi, and E. Larour, 2014: Deeply incised submarine glacial valleys beneath the Greenland ice sheet. *Nat. Geosci.*, **7**, 418–422, <https://doi.org/10.1038/ngeo2167>.

- Muglia, J., and A. Schmittner, 2015: Glacial Atlantic overturning increased by wind stress in climate models. *Geophys. Res. Lett.*, **42**, 9862–9868, <https://doi.org/10.1002/2015GL064583>.
- Müller, S. A., F. Joos, N. R. Edwards, and T. F. Stocker, 2006: Water mass distribution and ventilation time scales in a cost-efficient, three-dimensional ocean model. *J. Climate*, **19**, 5479–5499, <https://doi.org/10.1175/JCLI3911.1>.
- Nguyen, A. T., D. Menemenlis, and R. Kwok, 2009: Improved modeling of the arctic halocline with a subgrid-scale brine rejection parameterization. *J. Geophys. Res.*, **114**, C11014, <https://doi.org/10.1029/2008JC005121>.
- NOAA, 2009: ETOPO1 1 Arc-minute global relief model. NOAA National Centers for Environmental Information, accessed 20 November 2022, <https://www.ncei.noaa.gov/access/metadata/landing-page/bin/iso?id=gov.noaa.ngdc.mgg.dem:316>.
- Osman, M. B., J. E. Tierney, J. Zhu, R. Tardif, G. J. Hakim, J. King, and C. J. Poulsen, 2021: Globally resolved surface temperatures since the Last Glacial Maximum. *Nature*, **599**, 239–244, <https://doi.org/10.1038/s41586-021-03984-4>.
- Parekh, P., F. Joos, and S. A. Müller, 2008: A modeling assessment of the interplay between aeolian iron fluxes and iron-binding ligands in controlling carbon dioxide fluctuations during Antarctic warm events. *Paleoceanogr. Paleoclimatol.*, **23**, PA4202, <https://doi.org/10.1029/2007PA001531>.
- Paterson, W. S. B., 1994: *Physics of Glaciers*. 3rd ed. Pergamon, 480 pp.
- Peltier, W. R., D. F. Argus, and R. Drummond, 2015: Space geodesy constrains ice age terminal deglaciation: The global ICE-6G_C (VM5a) model. *J. Geophys. Res. Solid Earth*, **120**, 450–487, <https://doi.org/10.1002/2014JB011176>.
- Pfister, P. L., and T. F. Stocker, 2016: Earth system commitments due to delayed mitigation. *Environ. Res. Lett.*, **11**, 014010, <https://doi.org/10.1088/1748-9326/11/1/014010>.
- , and —, 2017: State-dependence of the climate sensitivity in Earth system models of intermediate complexity. *Geophys. Res. Lett.*, **44**, 10643–10653, <https://doi.org/10.1002/2017GL075457>.
- Pico, T., J. X. Mitrovica, K. L. Ferrier, and J. Braun, 2016: Global ice volume during MIS 3 inferred from a sea-level analysis of sedimentary core records in the Yellow River Delta. *Quat. Sci. Rev.*, **152**, 72–79, <https://doi.org/10.1016/j.quascirev.2016.09.012>.
- Pittard, M. L., P. L. Whitehouse, M. J. Bentley, and D. Small, 2022: An ensemble of Antarctic deglacial simulations constrained by geological observations. *Quat. Sci. Rev.*, **298**, 107800, <https://doi.org/10.1016/j.quascirev.2022.107800>.
- Pöppelmeier, F., M. Gutjahr, P. Blaser, H. Schulz, F. Süfke, and J. Lippold, 2021a: Stable Atlantic deep water mass sourcing on glacial-interglacial timescales. *Geophys. Res. Lett.*, **48**, e2021GL092722, <https://doi.org/10.1029/2021GL092722>.
- , D. J. Janssen, S. L. Jaccard, and T. F. Stocker, 2021b: Modeling the marine chromium cycle: New constraints on global-scale processes. *Biogeosciences*, **18**, 5447–5463, <https://doi.org/10.5194/bg-18-5447-2021>.
- , J. Scheen, A. Jeltsch-Thömmes, and T. F. Stocker, 2021c: Simulated stability of the Atlantic meridional overturning circulation during the last glacial maximum. *Climate Past*, **17**, 615–632, <https://doi.org/10.5194/cp-17-615-2021>.
- , J. Lippold, P. Blaser, M. Gutjahr, M. Frank, and T. F. Stocker, 2022: Neodymium isotopes as a paleo-water mass tracer: A model-data reassessment. *Quat. Sci. Rev.*, **279**, 107404, <https://doi.org/10.1016/j.quascirev.2022.107404>.
- , D. Baggenstos, M. Grimmer, Z. Liu, J. Schmitt, H. Fischer, and T. F. Stocker, 2023a: The effect of past saturation changes on noble gas reconstructions of mean ocean temperature. *Geophys. Res. Lett.*, **50**, e2022GL102055, <https://doi.org/10.1029/2022GL102055>.
- , A. Jeltsch-Thömmes, J. Lippold, F. Joos, and T. F. Stocker, 2023b: Multi-proxy constraints on Atlantic circulation dynamics since the last ice age. *Nat. Geosci.*, **16**, 349–356, <https://doi.org/10.1038/s41561-023-01140-3>.
- Reeh, N., 1991: Parameterization of melt rate and surface temperature on the Greenland ice sheet. *Polarforschung*, **59**, 113–128.
- Rempfer, J., T. F. Stocker, F. Joos, J.-C. Dutay, and M. Siddall, 2011: Modelling Nd-isotopes with a coarse resolution ocean circulation model: Sensitivities to model parameters and source/sink distributions. *Geochim. Cosmochim. Acta*, **75**, 5927–5950, <https://doi.org/10.1016/j.gca.2011.07.044>.
- , —, —, and —, 2012: Sensitivity of Nd isotopic composition in seawater to changes in Nd sources and paleoceanographic implications. *J. Geophys. Res.*, **117**, C12010, <https://doi.org/10.1029/2012JC008161>.
- , —, —, J. Lippold, and S. L. Jaccard, 2017: New insights into cycling of ²³¹Pa and ²³⁰Th in the Atlantic Ocean. *Earth Planet. Sci. Lett.*, **468**, 27–37, <https://doi.org/10.1016/j.epsl.2017.03.027>.
- Ritz, S. P., T. F. Stocker, and F. Joos, 2011a: A coupled dynamical ocean-energy balance atmosphere model for paleoclimate studies. *J. Climate*, **24**, 349–375, <https://doi.org/10.1175/2010JCLI3351.1>.
- , —, and J. P. Severinghaus, 2011b: Noble gases as proxies of mean ocean temperature: Sensitivity studies using a climate model of reduced complexity. *Quat. Sci. Rev.*, **30**, 3728–3741, <https://doi.org/10.1016/j.quascirev.2011.09.021>.
- , —, J. O. Grimalt, L. Menviel, and A. Timmermann, 2013: Estimated strength of the Atlantic overturning circulation during the last deglaciation. *Nat. Geosci.*, **6**, 208–212, <https://doi.org/10.1038/ngeo1723>.
- Roche, D. M., C. Dumas, M. Bügelmayer, S. Charbit, and C. Ritz, 2014: Adding a dynamical cryosphere to iLOVECLIM (version 1.0): Coupling with the GRISLI ice-sheet model. *Geosci. Model Dev.*, **7**, 1377–1394, <https://doi.org/10.5194/gmd-7-1377-2014>.
- Romanou, A., and Coauthors, 2023: Stochastic bifurcation of the North Atlantic circulation under a mid-range future climate scenario with the NASA-GISS ModelE. *J. Climate*, **36**, 6141–6161, <https://doi.org/10.1175/JCLI-D-22-0536.1>.
- Roth, R., 2013: Modeling forcings and responses in the global carbon cycle-climate system: Past, present and future. Ph.D. dissertation, University of Bern, 232 pp.
- Rudels, B., E. P. Jones, U. Schauer, and P. Eriksson, 2004: Atlantic sources of the Arctic Ocean surface and halocline waters. *Polar Res.*, **23**, 181–208, <https://doi.org/10.3402/polar.v23i2.6278>.
- Rutt, I. C., M. Hagdorn, N. R. J. Hulton, and A. J. Payne, 2009: The Glimmer community ice sheet model. *J. Geophys. Res.*, **114**, F02004, <https://doi.org/10.1029/2008JF001015>.
- Schär, C., and Coauthors, 2020: Kilometer-scale climate models: Prospects and challenges. *Bull. Amer. Meteor. Soc.*, **101**, E567–E587, <https://doi.org/10.1175/BAMS-D-18-0167.1>.
- Schmittner, A., and G. D. Egbert, 2014: An improved parameterization of tidal mixing for ocean models. *Geosci. Model Dev.*, **7**, 211–224, <https://doi.org/10.5194/gmd-7-211-2014>.
- Slater, J. G., C. Jaupart, and D. Galson, 1980: The heat flow through oceanic and continental crust and the heat loss of

- the Earth. *Rev. Geophys.*, **18**, 269–311, <https://doi.org/10.1029/RG018i001p00269>.
- Shackleton, S., J. A. Menking, E. Brook, C. Buizert, M. N. Dyonisius, V. V. Petrenko, D. Baggenstos, and J. P. Severinghaus, 2021: Evolution of mean ocean temperature in Marine Isotope Stage 4. *Climate Past*, **17**, 2273–2289, <https://doi.org/10.5194/cp-17-2273-2021>.
- Steinacher, M., F. Joos, and T. F. Stocker, 2013: Allowable carbon emissions lowered by multiple climate targets. *Nature*, **499**, 197–201, <https://doi.org/10.1038/nature12269>.
- St. Laurent, L. C., H. L. Simmons, and S. R. Jayne, 2002: Estimating tidally driven mixing in the deep ocean. *Geophys. Res. Lett.*, **29**, 2106, <https://doi.org/10.1029/2002GL015633>.
- Stocker, T. F., 2013: *The Ocean as a Component of the Climate System*. 2nd ed. Elsevier, 3–30.
- , and S. J. Johnsen, 2003: A minimum thermodynamic model for the bipolar seesaw. *Paleoceanogr. Paleoclimatol.*, **18**, 1087, <https://doi.org/10.1029/2003PA000920>.
- , D. G. Wright, and L. A. Mysak, 1992: A zonally averaged, coupled ocean–atmosphere model for paleoclimate studies. *J. Climate*, **5**, 773–797, [https://doi.org/10.1175/1520-0442\(1992\)005<0773:AZACOA>2.0.CO;2](https://doi.org/10.1175/1520-0442(1992)005<0773:AZACOA>2.0.CO;2).
- Stouffer, R. J., and Coauthors, 2006: Investigating the causes of the response of the thermohaline circulation to past and future climate changes. *J. Climate*, **19**, 1365–1387, <https://doi.org/10.1175/JCLI3689.1>.
- Talley, L. D., J. L. Reid, and P. E. Robbins, 2003: Data-based meridional overturning streamfunctions for the global ocean. *J. Climate*, **16**, 3213–3226, [https://doi.org/10.1175/1520-0442\(2003\)016<3213:DMOSFT>2.0.CO;2](https://doi.org/10.1175/1520-0442(2003)016<3213:DMOSFT>2.0.CO;2).
- Terhaar, J., T. L. Frölicher, M. T. Aschwanden, P. Friedlingstein, and F. Joos, 2022: Adaptive emission reduction approach to reach any global warming target. *Nat. Climate Change*, **12**, 1136–1142, <https://doi.org/10.1038/s41558-022-01537-9>.
- Tierney, J. E., J. Zhu, J. King, S. B. Malevich, G. J. Hakim, and C. J. Poulsen, 2020: Glacial cooling and climate sensitivity revisited. *Nature*, **584**, 569–573, <https://doi.org/10.1038/s41586-020-2617-x>.
- Tschumi, T., 2009: Modeling the ocean’s contribution to past and future changes in global carbon cycling. Ph.D. thesis, University of Bern, 145 pp.
- , F. Joos, and P. Parekh, 2008: How important are Southern Hemisphere wind changes for low glacial carbon dioxide? A model study. *Paleoceanogr. Paleoclimatol.*, **23**, PA4208, <https://doi.org/10.1029/2008PA001592>.
- Waelbroeck, C., L. Labeyrie, E. Michel, J. C. Duplessy, J. F. McManus, K. Lambeck, E. Balbon, and M. Labracherie, 2002: Sea-level and deep water temperature changes derived from benthic foraminifera isotopic records. *Quat. Sci. Rev.*, **21**, 295–305, [https://doi.org/10.1016/S0277-3791\(01\)00101-9](https://doi.org/10.1016/S0277-3791(01)00101-9).
- Weaver, A. J., and Coauthors, 2001: The UVic Earth system climate model: Model description, climatology, and applications to past, present and future climates. *Atmos.–Ocean*, **39**, 361–428, <https://doi.org/10.1080/07055900.2001.9649686>.
- Willeit, M., A. Ganopolski, R. Calov, and V. Brovkin, 2019: Mid-Pleistocene transition in glacial cycles explained by declining CO₂ and regolith removal. *Sci. Adv.*, **5**, eaav7337, <https://doi.org/10.1126/sciadv.aav7337>.
- , —, A. Robinson, and N. R. Edwards, 2022: The Earth system model CLIMBER-X v1.0-Part 1: Climate model description and validation. *Geosci. Model Dev.*, **15**, 5905–5948, <https://doi.org/10.5194/gmd-15-5905-2022>.
- Wilmes, S.-B., A. Schmittner, and J. A. M. Green, 2019: Glacial ice sheet extent effects on modeled tidal mixing and the global overturning circulation. *Paleoceanogr. Paleoclimatol.*, **34**, 1437–1454, <https://doi.org/10.1029/2019PA003644>.
- Woodgate, R. A., 2018: Increases in the Pacific inflow to the Arctic from 1990 to 2015, and insights into seasonal trends and driving mechanisms from year-round Bering Strait mooring data. *Prog. Oceanogr.*, **160**, 124–154, <https://doi.org/10.1016/j.pocean.2017.12.007>.